

# Tectonics

## RESEARCH ARTICLE

10.1029/2018TC005268

### Key Points:

- Patterns in exhumation from new low-temperature thermochronology reflect Marlborough Fault deformation during the evolving Kaikōura orogeny
- Miocene exhumation limited to hanging walls indicates early thrust faulting and uplift, first in the Inland then in the Seaward Kaikōura Range
- Exhumation is rapid and widespread across the Marlborough Fault System after Pliocene onset of dextral faulting

### Supporting Information:

- Supporting Information S1

### Correspondence to:

A. R. Duvall,  
aduvall@uw.edu

### Citation:

Collett, C. M., Duvall, A. R., Flowers, R. M., Tucker, G. E., & Upton, P. (2019). The timing and style of oblique deformation within New Zealand's Kaikōura Ranges and Marlborough Fault System based on low-temperature thermochronology. *Tectonics*, 38, 1250–1272. <https://doi.org/10.1029/2018TC005268>

Received 4 AUG 2018

Accepted 26 FEB 2019

Accepted article online 5 MAR 2019

Published online 8 APR 2019

# The Timing and Style of Oblique Deformation Within New Zealand's Kaikōura Ranges and Marlborough Fault System Based on Low-Temperature Thermochronology

C. M. Collett<sup>1</sup>, A. R. Duvall<sup>1</sup> , R. M. Flowers<sup>2</sup> , G. E. Tucker<sup>2,3</sup> , and P. Upton<sup>4</sup> 

<sup>1</sup>Department of Earth and Space Sciences, University of Washington, Seattle, WA, USA, <sup>2</sup>Department of Geological Sciences, University of Colorado, Boulder, CO, USA, <sup>3</sup>Cooperative Institute for Research in Environmental Sciences (CIRES), University of Colorado Boulder, Boulder, CO, USA, <sup>4</sup>GNS Science, Lower Hutt, New Zealand

**Abstract** The ~150-km-wide dextral Marlborough Fault System and adjacent Kaikōura Mountains accommodate oblique convergence between the Pacific and Australian plates at the NE end of the South Island, New Zealand. Low-temperature thermochronology from this region places new limits on the timing and style of Marlborough faulting and mountain building. We sampled rocks for apatite and zircon (U-Th/He) and apatite fission track dating from a range of elevations spanning ~2 km within the Kaikōura Ranges, which stand high above the active Marlborough dextral faults. The data reveal Miocene cooling localized to hanging wall rocks, first along the Clarence Fault in the Inland Kaikōura Range, then along the Jordan Thrust in the Seaward Kaikōura Range, followed by widespread, rapid cooling reflected in all samples across the study area starting at ~5 Ma. Our results suggest that topographic relief in this region predates the onset of dextral faulting and that portions of the Marlborough Faults were once thrust faults that coincided with the early development of the transpressive plate boundary. We relate Pliocene to present rapid exhumation across the field site, including at low-elevation sample sites in Marlborough Fault foot walls, to seaward translation and overthrusting of crust atop the downgoing slab by dextral Marlborough Fault motion. Our results show that spatial and temporal patterns in exhumation reflect a complex and evolving deformation field in the Marlborough Fault System over the past ~25 million years of Kaikōura orogeny.

## 1. Introduction

The active New Zealand plate boundary serves as a type locality for investigating the tectonic, structural, and landscape response to oblique plate collision (e.g., Batt et al., 2000; Beaumont et al., 1996; Beavan et al., 1999; Davey et al., 1998; Kamp & Tippett, 1993; Koons, 1989; Little et al., 2002; Norris et al., 1990; Sutherland et al., 2000; Upton et al., 2009; Walcott, 1998). At this margin, the oblique-dextral Alpine Fault and ~150-km-wide Marlborough Fault System (MFS) accommodate convergence of the Australian and Pacific plates in a broad transform boundary that extends almost the length of New Zealand's South Island (Figure 1).

The MFS stretches across the northeast corner of the South Island at the transition from oblique subduction of oceanic Pacific crust along the Hikurangi margin to the north (Figure 1) to Alpine Fault transform faulting and continental convergence to the south (Barnes et al., 1998). The plate boundary interface at this transition zone is complex. Pacific lithosphere is imaged beneath the Marlborough region at 25- to 50-km depth (Eberhart-Phillips & Bannister, 2010; Eberhart-Phillips & Reyners, 1997; Figure 1), with active subduction ceasing south and east of Kaikōura where the Chatham Rise, a region of continental crust on the Pacific Plate, is too buoyant to subduct (~43°S, Figure 1 inset).

On land, in the upper plate, oblique convergence is currently accommodated on the roughly NE-SW striking dextral Marlborough Faults and the adjacent Inland and Seaward Kaikōura Range (IKR and SKR; summits of 2,885 and 2,608 m for Tapuae-o-Uenuku and Mount Manakau in the Inland and Seaward Ranges, respectively). The temporal and spatial extent of uplift, deformation, and faulting within the MFS as the Kaikōura orogeny developed remains unclear. Lack of structural marker horizons across the study site makes it difficult to determine the associated structures or the extent of preexisting topography.

In this study, we consider the timing and magnitude of exhumation recorded in the Kaikōura Mountains and the adjacent Marlborough region using low-temperature thermochronology, which places constraints

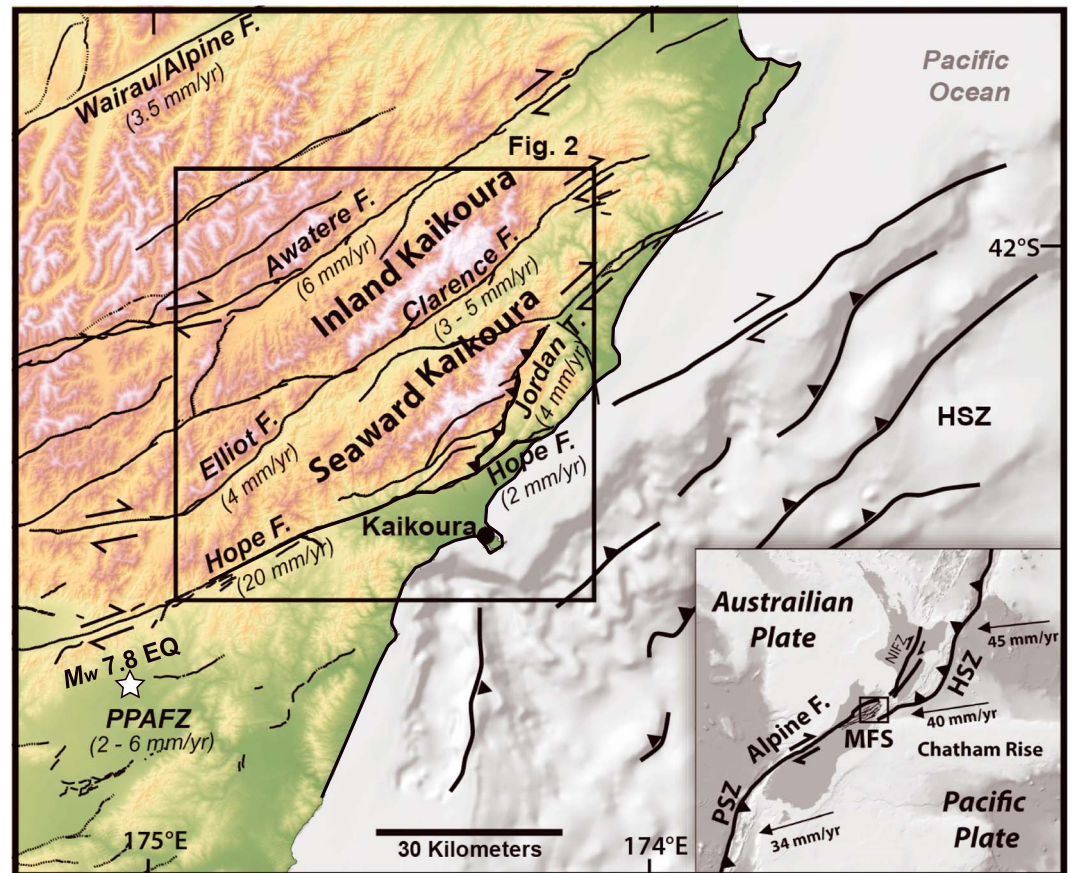


**Figure 1.** Study area location. Shaded relief map with elevation colored from low (green) to high (white), grayscale bathymetry, and faults simplified from 1:250,000 geological map of New Zealand (QMAP; Rattenbury et al., 2006). Geodetic slip rates of main Marlborough Faults shown in parentheses (Wallace et al., 2007). Black box outlines location of Figure 2. Star marks location of the epicentral area of the 14 November 2016  $M_w$  7.8 Kaikōura earthquake. PPAFZ = Porters Pass Amberly Fault Zone. Inset map depicts the broader Australian-Pacific plate boundaries. Small black square in inset map shows extent of main Figure 1. MFS = Marlborough Fault System; PSZ = Puysegur Subduction Zone; HSZ = Hikurangi Subduction Zone.

on the thermal history of rocks as they are exhumed toward Earth's surface. Due to the combination of strike-slip and dip-slip faulting in oblique tectonic settings, understanding the style and timing of deformation that has occurred can be challenging. The low-temperature thermochronology technique provides a useful means for understanding the deformation history in such transpressive and strike-slip systems around the world (e.g., Albino et al., 2014; Benowitz et al., 2011; Duvall et al., 2013; Herman et al., 2009; Leloup et al., 2001; Spotila et al., 1998, 2001).

With the new thermochronology data set, we interpret the timing and style of Marlborough faulting and adjacent Kaikōura Mountain uplift in the context of two related, outstanding questions: (1) Are the dextral Marlborough Faults reactivated early Miocene thrust faults (Lamb & Bibby, 1989; Rait et al., 1991; Randall et al., 2011; Vickery & Lamb, 1995)? and (2) Do patterns in exhumation reflect the late Miocene to early Pliocene onset of dextral faulting across the eastern MFS? We also consider how the timing and rate of exhumation compare between the IKR and SKR (and by proxy, the timing of faulting on the range-bounding faults). Because the MFS straddles the termination of Hikurangi subduction, what we learn from exhumation in this region offers important insight into the mechanics of slip transfer from a megathrust to continental transform faults.

## 2. Geologic Background and Tectonic Setting

The MFS includes four main oblique-dextral faults: the Wairau (the northern continuation of the Alpine Fault), Awatere, Clarence, and Hope (Figures 1 and 2). The Clarence and Elliot Faults (the latter a splay

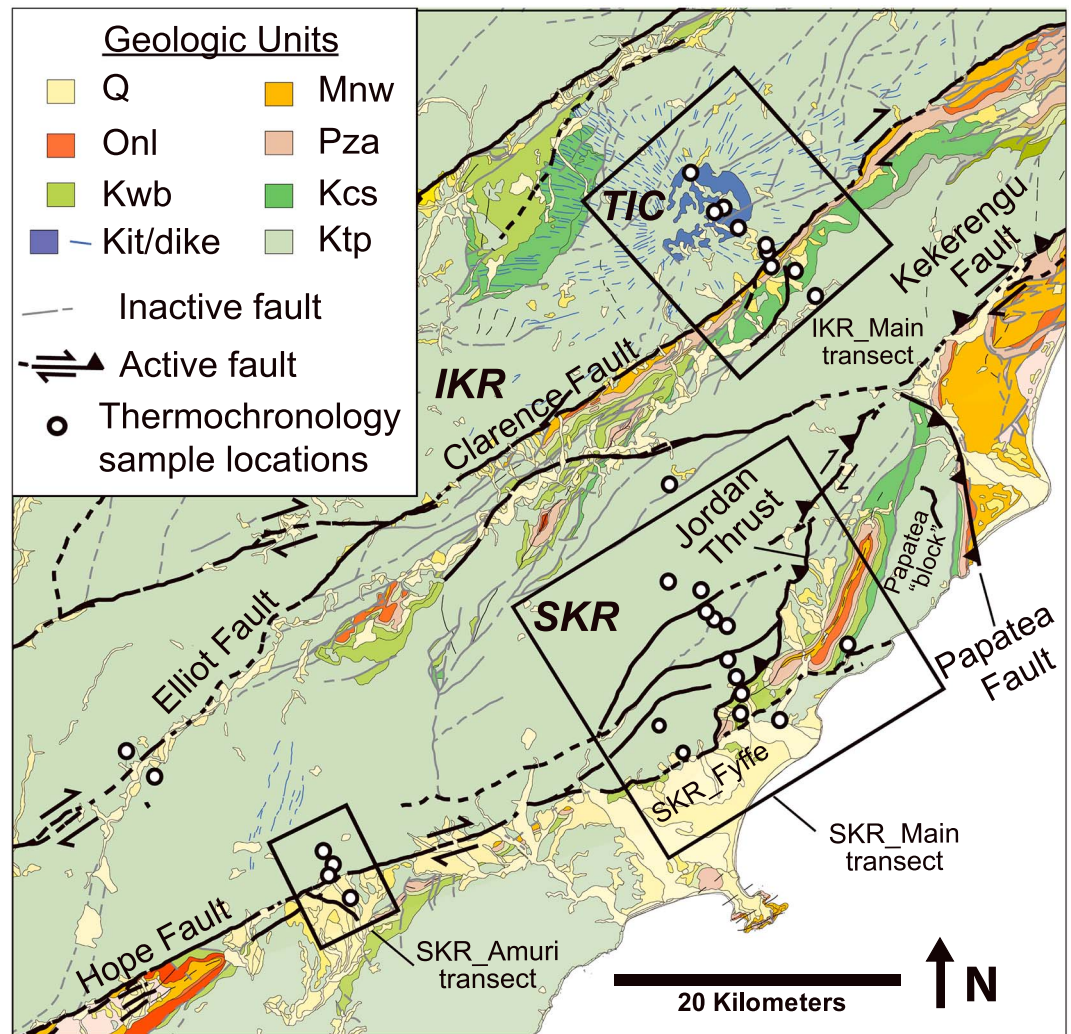


**Figure 2.** Geologic map of study area (Rattenbury et al., 2006) with thermochronology sample locations (white circles). Geologic units: Quaternary deposits (Q), Miocene Waima Formation mudstone and conglomerate (Mnw), Oligocene limestone (Onl), Paleogene Amuri limestone (Pza), Cretaceous Bluff sandstone (Kwb), Cretaceous Split Rock sandstone (Kcs), Cretaceous Tapuaenuku igneous complex (Kit), Cretaceous dikes (blue lines), and Cretaceous Torlesse Pahau terrane sandstone and mudstone (Ktp). IKR = Inland Kaikōura Range; SKR = Seaward Kaikōura Range; TIC = Mount Tapuae-o-Uenukuigneous complex.

of the Clarence Fault) bound the eastern IKR, and the Hope Fault, Jordan Thrust, and Kekerengu Fault bound the eastern SKR (Figure 2). Quaternary and Holocene offset markers and geodetic studies show horizontal fault slip rates of  $\sim 3\text{--}7$  mm/year for the Wairau, Awatere, and Clarence Faults (Benson et al., 2001; Cowan, 1989; Little et al., 1998; Little & Roberts, 1997; Mason et al., 2006; McCalpin, 1996; Nicol & Van Dissen, 2002; Van Dissen & Yeats, 1991; Wallace et al., 2007) and faster slip rates of  $\sim 20\text{--}25$  mm/year for the Hope Fault (Knuepfer, 1984, 1988; Langridge et al., 2003, 2010), whose displacement is thought to transfer northeastward onto the Jordan-Kekerengu system (Little et al., 2018; Van Dissen & Yeats, 1991).

With the exception of the Jordan Thrust, which dips  $\sim 35^\circ$ , the faults dip steeply ( $>60^\circ$ ) to the NW and range in strike from  $\sim 070^\circ$  along their western traces to  $\sim 055^\circ$  to the north and east (Lamb, 1988). This marked change in fault trend occurs approximately at the  $175^\circ\text{E}$  meridian and overlaps with the location of the subducted Pacific plate beneath Marlborough and the high topography of the Kaikōura Ranges. Fault segments with a more northerly strike are oblique to the plate motion vector and likely accommodate contraction (Little & Jones, 1998; Nicol & Van Dissen, 2002; Van Dissen & Yeats, 1991).

Van Dissen and Yeats (1991) proposed that the SKR may be actively rising since the Pliocene due to fault propagation folding on a previously blind, newly emergent Jordan Thrust. The IKR may share a similar style, where the Clarence fault exhibits oblique motion at depth and primarily strike-slip faulting at the free surface, resulting in dextral mapped offsets and broad hanging wall uplift (Nicol & Van Dissen, 2002). This type of “updip” strain partitioning has been proposed to apply to other faults in the Marlborough region as well (e.g., Bartholomew et al., 2014). Kaikōura Range topography may also relate to thrust faulting and range development during the early stages of plate collision (Baker & Seward, 1996; Brothers, 1974; Browne, 1995; King, 2000; Lamb, 2011; Lamb & Bibby, 1989; Lewis et al., 1980; Rait et al., 1991; Randall et al., 2011; Rattenbury et al., 2006; Walcott, 1978).

Significant rotation of the AUS-PAC plate boundary is known to have occurred over the lifespan of the Kaikōura orogeny, resulting in a major change in orientation of the Hikurangi subduction zone from an ~NW trend in the early Miocene to the ~NE trend of present day (Cande & Stock, 2004; King, 2000; Walcott, 1998). Geologic evidence suggests that the plate boundary zone widened around 8 to 5 Ma, with dextral motion initiating on the Marlborough Faults (Holt & Haines, 1995; Knuepfer, 1992; Little & Jones, 1998; Little & Roberts, 1997; Walcott, 1998) in a proposed north-to-south pattern. Because the Marlborough Faults ultimately link the Alpine Fault to the active Hikurangi subduction zone, southwestward migration of the Chatham Rise with respect to the Australian Plate is thought to have driven the southward propagation of faulting in Marlborough (Furlong, 2007; Furlong & Kamp, 2009; Little & Roberts, 1997; Wallace et al., 2007), with dextral motion on the Awatere Fault beginning around ~7 Ma (Little & Jones, 1998), on the Clarence Fault at ~3 Ma (Browne, 1992), and on the Hope Fault at ~1 Ma (Wood et al., 1994). The Wairau Fault, a continuation of the Alpine Fault, experienced a longer, protracted history of deformation beginning ~25 Ma and subsequently a much greater horizontal offset (~140-km total) than the other Marlborough Faults (~20–50 km of displacement; Anderson et al., 1993; Little & Jones, 1998; Mazengarb et al., 1993; Walcott, 1998).

As the plate boundary rotated, the Marlborough Faults may have changed orientation and their kinematics. Paleomagnetic, geodetic, and structural data from the MFS document clockwise vertical axis rotations of 50–130° relative to the Pacific Plate since ~20 Ma (Hall et al., 2004; Lamb, 2011; Lamb & Bibby, 1989; Little & Roberts, 1997; Randall et al., 2011; Vickery & Lamb, 1995) related to the locking of the subduction zone at the Chatham Rise (Little & Roberts, 1997). Some disagreement remains as to whether the large magnitude clockwise rotations affected all of the Marlborough Faults (Hall et al., 2004; Lamb, 2011; Lamb & Bibby, 1989; Randall et al., 2011) or was localized to coastal areas (Little & Roberts, 1997). Randall et al. (2011) argue for 80°+ of rotation of a coherent block that included the inland Marlborough Faults, which they interpret to have been thrust faults with a NW-SE strike early in the Miocene that rotated into their present NE-SW, dextral fault sense over the past 20 million years. Little and Roberts (1997) find evidence of large magnitude (100°+) clockwise rotation limited to the eastern end of the Clarence Fault, without substantial rotation of inland fault segments.

### 3. Methods and Approach

In this study, we use low-temperature thermochronometry from samples spanning the relief of the Kaikōura Mountains, both along strike and on opposite sides of faults, to help constrain the timing and magnitude of exhumation as an indirect proxy for Kaikōura mountain building and Marlborough Fault-related deformation. We rely primarily on the apatite (U-Th)/He thermochronometer (AHe) but utilize the higher-closure temperature zircon (U-Th)/He (ZHe) and apatite fission track (AFT) chronometers on a selection of samples to constrain a wider range of thermal histories. Apatite and zircon minerals have He closure temperatures of ~55–90 °C and ~200 to <50 °C, respectively, depending on grain size, cooling rate, and radiation damage (Dodson, 1973; Farley, 2000; Flowers et al., 2009; Guenther et al., 2013; Reiners et al., 2002, 2004; Shuster et al., 2006; Wolf et al., 1996). Fission tracks are retained in apatite crystals at temperatures below ~100–120 °C (Gleadow & Duddy, 1981; Ketcham et al., 2007). The relatively low closure temperatures of the AHe, AFT, and ZHe systems typically record exhumation through the uppermost crust and as a result provide the best means to determine the timing and rates of exhumation related to shallow crustal processes such as mountain building and faulting (e.g., Batt & Braun, 1999; Benowitz et al., 2011; Carrapa et al., 2011; Clark et al., 2010; Colgan et al., 2006; Duvall et al., 2013; Fitzgerald & Gleadow, 1990; Herman et al., 2009;

**Table 1**  
*Sample Descriptions*

Location	Sample ID	Lithology	Latitude	Longitude	Elevation (m)	No. of AHe	No. of AFT	No. of ZHe
Seaward Kaikōura Range								
SKR_Amuri								
Hope F. fw	12MFS11	eK Pahau gw.	−42.42	173.36	402	4	—	1
Hope F. hw	12MFS09	eK Pahau gw.	−42.41	173.34	478	3	—	4
Hope F. hw	12MFS08	eK Pahau gw.	−42.40	173.35	759	2	—	2
Hope F. hw	12MFS07	eK Pahau gw.	−42.39	173.34	1,118	1	—	2
SKR_Fyffe								
Hope F. hw	13MF07	eK Pahau gw.	−42.33	173.63	457	3	—	4
Hope F. hw	13MF01	eK Pahau gw.	−42.31	173.61	1,596	4	—	5
SKR_Main								
Hope F. fw	16MFS02	eK Pahau gw.	−42.31	173.72	65	5	—	3
Jordan T. fw	16MFS06	IK Split rock ss.	−42.26	173.77	127	—	37	—
Jordan T. fw	13MF10	IK Bluff ss.	−42.30	173.68	159	—	—	4
Jordan T. fw	16MFS05	IK Bluff ss.	−42.29	173.69	171	4	—	3
Jordan T. hw	13MF11	eK Pahau gw.	−42.28	173.68	219	4	38	5
Jordan T. hw	14MAN04	eK Pahau gw.	−42.25	173.67	698	3	—	—
Jordan T. hw	14MAN03	eK Pahau gw.	−42.25	173.66	1162	3	—	—
Jordan T. hw	14MAN02	eK Pahau gw.	−42.24	173.66	1,562	4	—	—
Jordan T. hw	15MAN07	eK Pahau gw.	−42.23	173.65	2,120	2	—	—
Jordan T. hw	15MAN06	eK Pahau gw.	−42.22	173.62	2,494	3	27	3
SKR backside	15CLA03	eK Pahau gw.	−42.16	173.63	856	2	—	3
Inland Kaikōura Range								
IKR_Elliot								
Elliot F. fw	15CLA01	eK Pahau gw.	−42.34	173.19	913	3	—	3
Elliot F. hw	15CLA02	eK Pahau gw.	−42.33	173.19	857	3	—	3
IKR_Main								
Clarence F. fw	15TAP07	eK Pahau gw.	−42.05	173.74	278	5	—	3
Clarence F. fw	15TAP06	IK Split rock ss.	−42.03	173.72	447	3	—	3
Clarence F. fw	15TAP05AB	M Waima cg.	−42.02	173.70	890	4	—	—
Clarence F. hw	15TAP04	eK Pahau gw.	−42.02	173.70	996	2	—	3
Clarence F. hw	15TAP03	eK Tapuaenuku dike	−42.01	173.70	1,278	2	—	—
Clarence F. hw	15TAP01	eK Tapuaenuku ig.	−42.00	173.68	2,046	—	—	3
Clarence F. hw	15TAP09	eK Tapuaenuku ig.	−41.99	173.67	2,601	3	—	—
Clarence F. hw	15TAP08	eK Tapuaenuku ig.	−41.99	173.66	2,811	—	—	2
IKR backside	14238	eK Tapuaenuku ig.	−41.97	173.64	1,350	3	—	—

*Note.* Seaward (SKR) and Inland Kaikōura (IKR) Range sample locations and lithologies with number of Apatite He (AHe), Apatite Fission Track (AFT), and Zircon He (ZHe) replicates. eK = early Cretaceous; IK = late Cretaceous; M = Miocene; fw = foot wall; hw = hanging wall; gw = greywacke; ss = sandstone; cg = conglomerate; ig = igneous.

Kirby et al., 2002; Little et al., 2005; Metcalf et al., 2009; Reiners et al., 2003; Spotila et al., 1998, 2001; Wagner & Reimer, 1972).

### 3.1. Sampling Approach

We collected a total of 28 samples by foot, raft, and helicopter across the field site (Figure 2). Twenty-four of these samples were analyzed for AHe, 19 for ZHe, and 3 for AFT (Table 1). The samples were collected mainly from the early Cretaceous Pahau greywacke terrane of the Torlesse composite terrane, with five collected from the early Cretaceous Tapuae-o-Uenuku Igneous Complex, four from late Cretaceous sandstones of the Bluff and Split Rock formations, and one from the Miocene Great Marlborough Conglomerate/Waima Formation (Table 1; more details on site stratigraphy in supporting information). These samples cover a broad area (>2,000 km<sup>2</sup>) and wide range in elevation (~100–3,000 m) within both the Seaward and Inland Ranges.

We sampled outcrops at similar elevations on either side of the range-bounding faults (Elliot and main strands of the Clarence Fault, the Hope Fault, and the Jordan Thrust) at multiple locations along fault strike to consider the timing and magnitude of vertical deformation at the mountain front and to check for any spatial variability in exhumation patterns. To assess the longer history of mountain building and spatial patterns

of growth, we also collected samples up steep relief elevation transects. Many studies have demonstrated the applicability of elevation transects and the “age-elevation relationship” in constraining long-term exhumation histories of mountains and the timing of adjacent faulting (e.g., Fitzgerald et al., 1995; Fitzgerald & Gleadow, 1990; Reiners et al., 2003; Wagner & Reimer, 1972). Plots of sample age versus elevation or depth can reveal apparent exhumation rates through time where breaks in slope represent changes in apparent erosion rate. Transitions from slow to fast rates likely relate to the initiation of mountain building, and by proxy, the onset of faulting. Comparison of single ages with multiple chronometers and age-elevation relationships between the IKR and SKR allow us to consider spatial patterns in exhumation timing, magnitude, and rate across the study site.

Three elevation transects were collected within the SKR along with a single sample from the NW (back) side of the range (Figure 2). The main transect (SKR\_Main) drapes the steep, southeast side of the range and crosses the range-bounding Jordan thrust (Figure 2). The ten samples along this transect cover over 2,200 m of elevation, extending from Mount Manakau, the highest peak in the SKR, extending from Mount Manakau, the highest peak in the SKR, to the Kaikōura coastal plain adjacent to the Pacific Ocean. The samples along this transect were analyzed for AHe (9), ZHe (5) and AFT (3). A second, smaller transect (SKR\_Fyffe) includes two samples (two AHe and two ZHe) within the neighboring ~1,100-m relief Mount Fyffe block near the intersection of the Hope and Jordan Faults (Figure 2). The third transect (SKR\_Amuri), located ~30 km SW of the other two transects, crosses the Hope Fault at the Charwell River and includes four samples (four AHe and four ZHe) that cover ~700 m of relief within the Amuri Range (Figure 2).

One elevation transect was collected within the Inland Kaikōura Mountains, along with two samples from either side of the Elliot strand of the Clarence Fault (IKR\_Elliot), ~40 km along strike (Figure 2). The IKR\_Main transect includes eight samples (six AHe and five ZHe) that cover >2,500 m of relief and extend across the SE flank of the mountain range from the top of Mount Tapuae-o-Uenuku to the floor of the adjacent Clarence river valley (Figure 2). An additional sample collected by Baker and Seward (1996) from the back (NW) side of the IKR was also analyzed for AHe.

### 3.2. Analytical Methods

Apatite and zircon minerals were separated from bedrock samples using standard mineral separation methods at the University of Washington, Central Washington University, and at GeoSep Services in Moscow, Idaho. AHe and ZHe analyses and age determinations were carried out at the University of Colorado Boulder Thermochronology Research and Instrumentation Laboratory. Individual mineral grains were handpicked, measured, and inspected for size, shape, and inclusions under ethanol with transmitted and polarized light using a Leica M205 C microscope at the University of Washington. Single grains (approximately three to five grains per sample) were packed into individual Niobium tubes and heated with a diode laser to extract radiogenic  $^4\text{He}$ . The degassed  $^4\text{He}$  was spiked with  $^3\text{He}$  and analyzed on a quadrupole mass spectrometer. This procedure was repeated at least once to ensure complete mineral degassing. Degassed grains were removed from the line and spiked with a calibrated  $^{235}\text{U}$ - $^{230}\text{Th}$ - $^{145}\text{Nd}$  mixture. Apatite grains were dissolved in  $\text{HNO}_3$  for 2 hr at 80 °C. Zircon samples were dissolved using Parr large-capacity dissolution vessels through a multistep acid vapor HF and HCl dissolution process. The U, Th, Nd, and Sm of dissolved samples were measured on a Thermo-Finnigan Element 2 magnetic sector ICP-MS at the University of Colorado Boulder.

Raw dates were determined from the He, U, Th, and Sm measurements and corrected for alpha ejection using the methods of Ketchum et al. (2011). The uncertainty of individual AHe and ZHe dates includes the propagated error on the U, Th, Sm, and He measurements and is reported at  $2\sigma$ . Mean dates were calculated from the corrected sample replicates, and uncertainties on the mean are reported as  $2\sigma$  standard deviation on the mean in bold in Tables 2 and 3. Of the 175 analyzed apatites, we exclude 38 grains with the following characteristics. First, we discarded those that did not degas 99% of the total He extracted upon first heating (reextracts), implying possible zircon inclusions that may bias the dates. The hazy character of the detrital apatites from the sedimentary samples made inclusions more difficult to avoid during picking than in apatites from typical igneous samples. Second, we eliminated grains with effective Uranium concentrations ( $eU$ ) < 5 ppm, as many of these had anomalously old ages likely due to implantation effects from U- and Th-bearing neighbors (e.g., Murray et al., 2014; Spiegel et al., 2009). Third, we excluded replicate

**Table 2**  
*Apatite Helium Ages*

Location	Sample ID	Dim mass (µg)	$r_s$ (µm) <sup>a</sup>	4He (nmol/g)	U (ppm)	Th (ppm)	Sm (ppm)	Raw date (a)	Ft	Date (Ma) <sup>b</sup>	2σ (Ma) <sup>c</sup>
SKR_Main	16MFS02_a01	1.33	40.04	0.29	13.56	60.18	13.04	1.9	0.63	3.0	0.2
	16MFS02_a02	0.67	33.56	0.38	10.18	47.53	32.49	3.2	0.56	5.7	0.6
	16MFS02_a03	1.10	39.80	0.44	21.87	60.56	28.51	2.2	0.64	3.4	0.2
	16MFS02_a04	1.25	42.11	0.21	9.42	24.23	41.96	2.5	0.66	3.8	0.4
	16MFS02_a05	1.06	39.44	0.49	14.76	59.34	64.53	3.1	0.63	4.8	0.1
Jordan T. hw	16MFS05_a01 <sup>d</sup>	0.79	36.09	5.25	12.88	21.01	20.11	53.9	0.61	4.1	1.1
	16MFS05_a02	1.51	41.46	0.53	26.91	94.30	13.48	2.0	0.64	3.1	0.2
	16MFS05_a03	1.06	39.34	0.96	52.39	167.85	38.59	1.9	0.63	3.1	0.2
	16MFS05_a04	0.94	37.90	0.32	10.09	35.82	37.46	3.2	0.62	5.1	0.4
	16MFS05_a05	0.84	36.96	1.11	28.12	150.01	81.08	3.2	0.60	5.3	0.2
Jordan T. hw	13MF11_aA	2.86	59.05	0.12	8.84	25.82	16.36	1.4	0.74	1.9	0.2
	13MF11_aB	2.11	49.70	0.05	4.51	19.80	27.46	1.0	0.69	1.4	0.2
	13MF11_aC	0.90	37.12	0.79	81.03	4.46	24.49	1.8	0.63	2.8	0.2
	13MF11_aD	0.64	33.51	0.14	13.33	30.15	30.97	1.3	0.57	2.3	0.4
	13MF11									2.1	0.6
Jordan T. hw	14MAN04_aA	1.66	40.34	2.80	18.17	12.91	8.67	24.4	0.65	37.2	2.2
	14MAN04_aC	0.68	32.25	0.49	79.60	115.08	16.70	0.9	0.57	1.5	0.1
	14MAN04_aD	0.67	32.75	13.60	89.67	33.52	71.19	25.7	0.58	43.9	1.4
	14MAN04									27.5	22.8
Jordan T. hw	14MAN03_aA <sup>d</sup>	0.99	36.76	0.54	3.42	33.93	45.03	8.5	0.60	14.0	2.2
	14MAN03_aB	0.55	30.14	0.94	26.97	113.62	136.87	3.2	0.53	5.9	1.0
	14MAN03_aC	0.45	28.44	0.23	29.12	79.33	38.11	0.9	0.51	1.7	0.1
	14MAN03_aE	0.57	30.77	0.28	42.70	78.43	44.16	0.8	0.55	1.5	0.1
	14MAN03									3.0	2.5
Jordan T. hw	14MAN02_aA	1.30	37.88	0.22	9.83	72.15	54.80	1.5	0.60	2.5	0.2
	14MAN02_aB	2.55	49.89	0.10	6.87	38.42	25.19	1.1	0.70	1.6	0.2
	14MAN02_aC	1.48	43.57	0.21	8.20	47.34	70.39	2.0	0.66	3.0	0.2
	14MAN02_aE <sup>d</sup>	1.04	39.67	0.56	11.16	72.36	65.13	3.6	0.63	5.7	0.4
	14MAN02									2.4	0.7
Jordan T. hw	15MAN07_aA	0.75	33.53	0.40	44.90	75.18	24.86	1.2	0.59	2.0	0.2
	15MAN07_aD	1.26	39.67	0.16	6.13	37.29	44.75	2.0	0.63	3.1	0.4
	15MAN07									2.6	0.8
	15MAN06_aA	1.58	43.20	0.08	3.95	29.07	26.69	1.4	0.66	2.1	0.4
	15MAN06_aB	0.82	34.67	0.15	14.96	84.09	48.02	0.8	0.58	1.3	0.2
Jordan T. hw	15MAN06_aC	0.94	36.35	1.32	###	151.13	26.33	1.5	0.62	2.5	0.1
	15MAN06_aD	0.99	37.12	0.23	16.47	64.78	55.82	1.3	0.61	2.1	0.2
	15MAN06_aE <sup>d</sup>	0.67	32.28	1.00	34.90	144.04	40.01	2.7	0.56	4.8	0.2
	15MAN06									2.0	0.5
	15CLA03_aA	1.44	41.68	0.07	10.45	40.54	17.16	0.7	0.65	1.0	0.2
SKR backside	15CLA03_aB	1.33	40.90	0.10	6.52	23.40	6.04	1.6	0.65	2.5	0.4
	15CLA03									1.8	1.1
	SKR_Fyffe										
Hope F. hw	13MF07_aA	1.86	50.13	0.12	5.11	24.76	56.07	2.0	0.69	2.9	0.4
	13MF07_aB	2.25	50.31	1.12	93.32	11.98	47.12	2.1	0.71	3.0	0.2

Seaward Kaikoura Range

Table 2 (continued)

Location	Sample ID	Dim mass ( $\mu\text{g}$ )	$r_s$ ( $\mu\text{m}$ ) <sup>a</sup>	4He (nmol/g)	U (ppm)	Th (ppm)	Sm (ppm)	Raw date (a)	Ft	Date (Ma) <sup>b</sup>	$2\sigma$ (Ma) <sup>c</sup>
457-m elevation	13MF07_B	1.11	39.86	0.16	5.71	47.97	13.49	1.7	0.61	2.8	0.4
	13MF07_E <sup>d</sup>	1.24	40.42	0.57	49.74	136.85	11.91	1.3	0.60	2.2	0.1
	<b>13MF07</b>									<b>2.9</b>	<b>0.1</b>
Hope F. hw	13MF01_aA	3.43	55.58	0.27	5.92	26.42	27.39	4.0	0.73	5.4	0.2
	13MF01_aB	4.73	61.41	0.37	16.72	62.76	9.06	2.1	0.76	2.8	0.1
	13MF01_aC	1.63	43.85	0.34	12.74	68.38	59.46	2.1	0.67	3.2	0.2
	13MF01_aD <sup>d</sup>	3.15	56.72	0.44	6.32	27.24	30.24	6.3	0.74	8.5	0.2
	13MF01_aE	5.60	67.67	0.13	5.25	27.33	25.64	2.0	0.78	2.6	0.2
	<b>13MF01</b>									<b>3.5</b>	<b>1.3</b>
SKR_Amuri											
Hope F. fw	12MFS11_aB	0.69	32.65	0.04	1.58	15.20	29.41	1.5	0.55	2.6	1.8
	12MFS11_aC	0.63	31.38	0.15	8.24	67.31	62.95	1.1	0.54	2.1	0.4
402-m elevation	12MFS11_aD	1.21	39.13	0.07	7.82	36.36	29.00	0.7	0.63	1.2	0.2
	12MFS11_aE	2.27	48.08	0.10	10.17	29.66	29.97	1.0	0.70	1.5	0.2
	<b>12MFS11</b>									<b>1.9</b>	<b>0.6</b>
Hope F. hw	12MFS09_aB	1.60	46.15	0.65	68.52	61.41	47.32	1.5	0.68	2.1	0.1
	12MFS09_aC	1.17	42.26	0.20	20.40	27.16	73.34	1.4	0.67	2.0	0.2
478-m elevation	12MFS09_aD	4.94	67.21	0.20	6.42	28.40	18.66	2.8	0.77	3.6	0.2
	<b>12MFS09</b>									<b>2.6</b>	<b>0.9</b>
Hope F. hw	12MFS08A	5.35	65.77	0.11	4.31	18.70	19.95	2.2	0.75	2.9	4.2
759-m elevation	12MFS08_aB	4.21	61.29	0.33	4.07	13.87	21.30	8.1	0.75	10.7	0.8
	<b>12MFS08</b>									<b>6.8</b>	<b>5.5</b>
Hope F. hw	12MFS07_aC	4.09	59.50	0.80	27.04	88.35	12.77	3.1	0.75	4.1	0.3
	<b>12MFS07</b>									<b>4.1</b>	<b>0.3</b>
Inland Kaikōura Range											
IKR_Main	15TAP07_aA	0.86	35.31	0.13	5.92	32.91	27.28	1.7	0.59	2.8	0.6
	15TAP07_aB	0.93	36.11	0.35	43.72	19.96	74.06	1.3	0.63	2.1	0.2
Clarence F. fw	15TAP07_aC	0.59	30.98	0.42	49.73	110.31	94.63	1.0	0.56	1.8	0.2
	15TAP07_aD	0.66	31.68	0.08	10.23	17.51	50.54	1.0	0.56	1.7	0.5
278-m elevation	15TAP07_aE	1.09	34.72	0.18	35.17	85.22	19.40	0.6	0.59	1.0	0.2
	<b>15TAP07</b>									<b>1.9</b>	<b>0.7</b>
Clarence F. fw	15TAP06_aB	4.05	59.03	0.46	6.04	27.47	25.32	6.6	0.74	8.9	0.6
	15TAP06_aC <sup>d</sup>	2.26	48.54	1.15	4.74	21.70	27.80	21.1	0.70	30.1	1.4
447-m elevation	15TAP06_aD	2.89	52.99	0.28	4.29	24.67	34.93	5.0	0.72	6.9	0.4
	15TAP06_aE	1.57	45.46	0.34	6.12	28.89	49.85	4.7	0.67	6.8	0.6
	<b>15TAP06</b>									<b>7.5</b>	<b>1.2</b>
Clarence F. fw	15TAP05AB_aA	1.03	37.04	2.66	18.51	45.87	38.16	16.6	0.62	26.7	0.8
	15TAP05AB_aB	0.69	32.37	2.79	20.60	51.67	35.57	15.6	0.57	27.3	1.0
890-m elevation	15TAP05AB_aC	0.82	35.07	2.55	16.16	48.40	43.35	16.9	0.59	28.6	1.4
	15TAP05AB_aD	0.63	33.60	2.21	13.96	46.29	73.79	16.1	0.58	27.4	0.6
	15TAP05AB_aE <sup>d</sup>	2.86	49.90	0.55	4.10	22.58	25.79	10.6	0.70	15.1	1.2
	<b>15TAP05AB</b>									<b>27.5</b>	<b>1.0</b>
Clarence F. hw	15tap04_aC	0.69	30.69	0.19	2.16	19.22	23.70	5.0	0.53	9.4	2.2
	15tap04_aD	1.02	37.33	0.18	5.74	29.70	11.46	2.5	0.61	4.1	0.6
	<b>15TAP04</b>									<b>6.8</b>	<b>3.7</b>
Clarence F. hw	15TAP03_aB	0.31	26.42	0.31	14.32	85.62	73.65	1.6	0.46	3.5	0.6
	15TAP03_aC	0.51	29.47	0.19	9.50	43.16	37.25	1.7	0.52	3.3	0.6
	<b>15TAP03</b>									<b>3.4</b>	<b>0.1</b>



**Table 2 (continued)**

Location	Sample ID	Dim mass ( $\mu\text{g}$ )	$r_s$ ( $\mu\text{m}$ ) <sup>a</sup>	<sup>4</sup> He (nmol/g)	U (ppm)	Th (ppm)	Sm (ppm)	Raw date (a)	Ft	Date (Ma) <sup>b</sup>	$2\sigma$ (Ma) <sup>c</sup>
Clarence F. hw 2,601-m elevation	15TAP09_aB	7.27	71.22	0.28	5.30	19.67	17.41	5.2	0.79	6.5	0.2
	15TAP09_aC	3.23	53.85	0.47	8.79	38.12	28.89	4.8	0.73	6.6	0.2
	15TAP09_aD	1.46	41.91	1.14	7.90	44.56	45.89	11.2	0.65	17.1	1.2
IKR backside 1,350-m elevation	<b>15TAP09</b>									<b>10.1</b>	<b>6.1</b>
	14238_aB	1.21	39.25	0.31	4.55	18.44	40.66	6.3	0.64	9.8	0.8
	14238_aD	1.95	35.35	0.18	2.97	12.61	23.97	5.5	0.60	9.0	1.2
	14238_aE	2.03	47.05	0.35	4.42	17.49	33.33	7.3	0.69	10.5	0.6
IKR_Elliott	<b>14238</b>									<b>9.8</b>	<b>0.8</b>
Elliot F. fw 913-m elevation	15CLA01_aA	1.06	37.20	1.23	27.08	22.27	26.94	7.0	0.64	11.0	0.4
	15CLA01_aC	1.86	43.59	0.32	6.86	17.09	26.03	5.4	0.68	7.9	0.6
	15CLA01_aD	1.55	41.07	1.88	94.13	105.70	33.68	2.9	0.66	4.4	0.1
	15CLA01_aE <sup>d</sup>	1.13	38.79	1.70	9.43	42.94	31.91	15.8	0.63	25.1	1.0
Elliot F. hw 857-m elevation	<b>15CLA01</b>									<b>7.8</b>	<b>3.3</b>
	15CLA02_aA <sup>d</sup>	0.74	33.32	8.68	44.25	81.80	7.99	25.2	0.59	43.0	0.8
	15CLA02_aC	0.60	32.59	0.82	68.36	78.28	57.76	1.7	0.57	3.0	0.2
	15CLA02_aD	0.86	34.12	0.33	11.48	36.83	39.17	3.0	0.58	5.1	0.4
	15CLA02_aE	0.38	28.08	0.28	18.40	51.60	133.70	1.6	0.50	3.2	0.4
	<b>15CLA02</b>									<b>3.8</b>	<b>1.2</b>

Note. The 2 sigma standard deviation on the mean is in bold. fw = foot wall; hw = hanging wall.

<sup>a</sup> $r_s$  is the equivalent spherical radius. <sup>b</sup>Mean sample age. <sup>c</sup>The 2 sigma analytical uncertainty on each replicate age. <sup>d</sup>Replicate excluded from mean age determination due to failure of Pierce's outlier test (Ross, 2003).

**Table 3**  
*Zircon Helium Ages*

Location	Sample ID	Dim mass (mg)	$r_s$ ( $\mu\text{m}$ ) <sup>a</sup>	4He (nmol/g)	U (ppm)	Th (ppm)	Sm (ppm)	Raw date (Ma)	Ft	Date (Ma) <sup>b</sup>	$2\sigma$ (Ma) <sup>c</sup>
Seaward Kaikōura Range											
SKR_Main:	16MFS02_z1	4.37	52.05	256.66	225.98	178.59	8.61	175.0	0.78	223.4	5.0
Hope F. fw	16MFS02_z2	2.50	41.35	288.73	287.78	143.49	8.84	164.2	0.73	224.1	2.9
65-m elevation	16MFS02_z3	3.38	45.92	154.69	151.03	51.55	0.00	173.2	0.76	228.2	3.0
	<b>16MFS02</b>									<b>225.2</b>	<b>2.6</b>
	13MF10_zA	4.43	49.19	136.89	226.82	194.16	—	92.4	0.77	119.9	0.1
	13MF10_zB	2.95	46.41	172.91	183.51	35.71	—	164.8	0.76	215.9	0.4
Jordan T. hw	13MF10_zC	2.45	43.09	277.02	465.54	255.13	—	97.0	0.74	130.8	0.2
159-m elevation	13MF10_zD	2.14	40.64	110.48	95.64	79.67	—	176.4	0.72	242.9	0.2
	<b>13MF10</b>									<b>177.4</b>	<b>61.3</b>
	16MFS05_z1	1.81	38.22	301.00	350.77	285.14	0.00	132.1	0.71	186.3	2.1
Jordan T. hw	16MFS05_z2	2.17	40.76	79.11	81.66	69.45	49.95	147.2	0.72	202.6	4.2
171-melevation	16MFS05_z3	1.33	35.17	83.79	96.65	97.80	0.00	128.5	0.68	187.7	3.6
	<b>16MFS05</b>									<b>192.2</b>	<b>9.0</b>
	13MF11A	4.40	45.18	30.21	327.30	70.38	—	16.3	0.75	21.7	0.5
	13MF11B <sup>d</sup>	5.37	50.07	44.91	281.53	26.64	—	28.9	0.79	36.8	0.6
Jordan T. hw	13MF11C <sup>d</sup>	2.71	40.91	3.51	114.18	120.57	—	4.6	0.74	6.2	0.1
219-m elevation	13MF11D	9.97	65.36	16.56	170.26	66.65	—	16.5	0.84	19.7	0.4
	13MF11E	2.88	41.88	25.27	384.39	66.67	—	11.7	0.75	15.6	0.3
	<b>13MF11</b>									<b>19.0</b>	<b>3.1</b>
	15MAN06_zA	3.25	48.74	75.65	129.77	100.27	0.00	90.8	0.77	118.2	8.2
Jordan T. hw	15MAN06_zB	2.68	41.30	237.59	363.64	229.34	0.00	104.6	0.73	143.3	10.2
2,494-m elevation	15MAN06_zC	3.02	43.53	115.55	290.63	265.23	0.00	60.4	0.74	81.6	5.8
	<b>15MAN06</b>									<b>114.4</b>	<b>31.0</b>
	15CLA03_zA	6.43	57.38	252.72	397.31	74.06	0.11	112.0	0.80	139.1	2.0
SKR backside	15CLA03_zB	7.00	60.75	665.18	597.69	252.40	0.00	184.8	0.81	226.7	4.2
856-m elevation	15CLA03_zC	6.25	58.88	135.25	231.01	222.08	0.00	87.9	0.80	109.2	1.7
	<b>15CLA03</b>									<b>158.3</b>	<b>61.1</b>
SKR_Fyffe	13MF07A	2.85	40.54	6.41	129.96	77.28	—	8.0	0.72	11.1	0.5
	13MF07C	5.29	49.46	10.07	159.43	60.38	—	10.7	0.78	13.8	0.4
Hope F. hw	13MF07D	2.97	41.61	20.11	230.93	32.46	—	15.6	0.73	21.4	0.5
457-m elevation	13MF07_zA	3.72	49.62	8.66	115.54	92.49	—	11.7	0.77	15.2	1.1
	<b>13MF07</b>									<b>15.4</b>	<b>4.4</b>
	13MF01A	7.25	55.56	6.66	74.57	34.65	—	14.9	0.79	18.8	0.5
	13MF01B	10.63	63.08	17.40	202.30	94.13	—	14.4	0.81	17.6	0.4
Hope F. hw	13MF01C	13.53	71.38	10.46	234.07	151.45	—	7.2	0.85	8.5	0.2
1,596-m elevation	13MF01D	2.94	40.48	18.12	616.85	63.45	—	5.3	0.72	7.4	0.2
	13MF01E	3.52	45.00	13.91	315.52	80.89	—	7.7	0.77	10.1	0.2
	<b>13MF01</b>									<b>12.5</b>	<b>5.4</b>
SKR_Amuri	12MFS11_zA	9.09	62.53	196.82	125.29	46.46	—	261.9	0.82	318.3	6.1
Hope F. fw	<b>12MFS11</b>									—	—
402-m elevation	12MFS09A	5.33	46.23	296.52	371.11	28.61	—	143.8	0.76	190.4	3.4
	12MFS09B	14.99	69.79	87.42	67.50	40.51	—	206.8	0.85	243.9	6.2
Hope F. hw	12MFS09C	2.70	40.11	123.51	136.11	60.33	—	150.5	0.72	209.3	5.7
478-m elevation	12MFS09D	4.51	48.37	130.38	124.90	32.85	—	179.5	0.78	229.8	4.0
	<b>12MFS09</b>									<b>218.3</b>	<b>23.4</b>
Hope F. hw	12MFS08B	4.70	48.53	132.53	173.51	41.54	—	132.6	0.76	173.4	3.6
759-m elevation	12MFS08D	7.28	55.42	70.66	108.34	84.70	—	101.3	0.81	125.7	1.8
	<b>12MFS08</b>									<b>149.5</b>	<b>33.7</b>
Hope F. hw	12MFS07A	2.98	41.03	18.83	46.73	35.79	—	63.0	0.72	87.1	2.9
1,118-m elevation	12MFS07C	3.51	42.80	116.40	136.17	47.69	—	144.7	0.74	196.7	4.0
	<b>12MFS07</b>									<b>141.9</b>	<b>77.5</b>
Inland Kaikōura Range											
IKR_Main											
	15TAP07_zA	4.20	50.83	271.48	233.95	114.43	0.00	189.9	0.78	243.3	17.4
Clarence F. fw	15TAP07_zB	2.91	46.13	111.53	157.96	91.78	0.00	114.1	0.75	150.6	10.6

Table 3 (continued)

Location	Sample ID	Dim mass (mg)	$r_s$ ( $\mu\text{m}$ ) <sup>a</sup>	4He (nmol/g)	U (ppm)	Th (ppm)	Sm (ppm)	Raw date (Ma)	Ft	Date (Ma) <sup>b</sup>	$2\sigma$ (Ma) <sup>c</sup>
278-m elevation	15TAP07_zC	2.44	43.48	270.27	531.76	491.07	12.07	76.9	0.74	103.9	7.3
	<b>15TAP07</b>									<b>165.9</b>	<b>70.9</b>
Clarence F. fw	15TAP06_zA	6.11	56.97	66.03	102.07	88.61	0.00	98.8	0.80	123.6	8.7
	15TAP06_zB	10.11	66.25	210.76	289.10	296.81	0.00	107.9	0.82	130.7	9.3
447-m elevation	15TAP06_zC	7.13	59.58	615.96	732.92	301.75	0.91	140.4	0.81	173.1	12.3
	<b>15TAP06</b>									<b>142.5</b>	<b>26.8</b>
Clarence F. fw	15TAP04_zA	5.05	54.62	41.03	283.20	54.48	0.70	25.7	0.79	32.3	0.5
	15TAP04_zB	4.37	51.34	21.43	164.46	109.93	0.00	20.8	0.78	26.8	0.4
996-m elevation	15TAP04_zC	3.07	44.11	58.00	300.13	39.34	0.00	34.7	0.75	46.3	0.8
	<b>15TAP04</b>									<b>35.1</b>	<b>10.1</b>
Clarence F. hw	15TAP01_zA	17.97	73.29	93.21	226.65	222.28	0.75	61.6	0.84	73.1	5.2
	15TAP01_zB	20.81	75.75	89.01	209.04	230.05	0.74	62.4	0.85	73.7	5.2
2,046-m elevation	15TAP01_zC	19.82	79.57	50.72	132.86	125.55	0.38	57.6	0.85	67.5	4.8
	<b>15TAP01</b>									<b>71.5</b>	<b>3.4</b>
Clarence F. hw	15TAP08_zA	10.70	59.10	334.60	495.92	863.82	7.99	88.0	0.80	109.8	17.0
	15TAP08_zC	1.78	43.08	411.28	681.66	####	6.38	73.8	0.68	108.6	8.1
IKR_Elliot	<b>15TAP08</b>									<b>109.2</b>	<b>0.8</b>
	15CLA01_zA	2.20	40.60	768.49	844.26	243.87	0.00	156.0	0.73	213.7	3.2
Elliot F. fw	15CLA01_zB	3.06	44.22	224.76	349.03	214.07	0.00	103.5	0.74	138.5	2.0
	15CLA01_zC	2.52	42.68	269.29	587.74	231.64	0.00	77.3	0.74	104.5	2.2
913-m elevation	<b>15CLA01</b>									<b>152.2</b>	<b>55.9</b>
	15CLA02_zA	1.49	37.45	34.03	762.14	392.32	5.56	7.4	0.70	10.5	0.1
Elliot F. hw	15CLA02_zB	3.61	45.15	179.71	790.61	231.96	3.95	39.3	0.75	52.2	0.8
	15CLA02_zC	2.75	43.55	28.99	500.59	108.73	4.73	10.2	0.74	13.7	0.2
857-m elevation	<b>15CLA02</b>									<b>25.5</b>	<b>23.2</b>

Note. The 2 sigma standard deviation on the mean is in bold. fw = foot wall; hw = hanging wall. <sup>a</sup> $r_s$  is the equivalent spherical radius. <sup>b</sup>Mean sample age. <sup>c</sup>The 2 sigma analytical uncertainty on each replicate age. <sup>d</sup>Replicate excluded from mean age determination due to failure of Pierce's outlier test (Ross, 2003).

grains deemed outliers using the Pierce criterion (Ross, 2003). We evaluated all samples for age versus  $eU$  correlations (which may develop owing to radiation damage effects on apatite He retentivity; e.g., Flowers et al., 2007, Shuster et al., 2006) and age versus grain size correlations (e.g., Reiners & Farley, 2001) but found no robust trends.

All AFT analyses were performed by GeoSep Services (GSS) with grains analyzed with a quadrupole ICP-MS at Apatite to Zircon, Inc. Ages were determined using a modified decay equation that includes calibration for the LA-ICP-MS using the Durango fluorapatite standard (Donelick et al., 2005). Pooled apatite AFT ages are reported (Galbraith & Laslett, 1993; Gallagher et al., 1998) with between 30 and 40 individual grains measured to estimate age and analytical error.

#### 4. Thermochronology Results

All measured ages are reported in Tables 2–4 and plotted in Figures 3 and 4. A general comparison of the cooling ages against the geologic age of sampled rocks shows that all AHe dates are reset (Figure 3), meaning that they are younger than the depositional age of the sample (or emplacement age, in the case of samples from the Tapuae-o-Uenuku Igneous Complex) and therefore require peak temperatures greater than  $\sim 70$  °C. In contrast, only some of the AFT and ZHe samples are younger than or overlap with deposition, and these are limited to hanging wall sites (Figure 3). Unreset AFT ages indicate peak temperatures less than  $\sim 110$  °C (for ZHe ages the accumulated radiation damage influences this temperature bound). Below, we compare ages from opposite fault blocks for each of the applied chronometers to assess relative magnitudes of exhumation in fault hanging walls and foot walls. We also describe trends in data along high-relief elevation transects modeled using QTQt thermal modeling software (Gallagher, 2012).

**Table 4**  
Fission Track Data

Location	Sample ID	Pooled age (Ma)	95%– CI (Ma)	95%+ CI (Ma)	No. of g rains	Mean Dpar (um)	No. of tracks	Mean (U; ppm)	Mean (Th; ppm)	Mean (Sm; ppm)	Chi square
Apatite fission track age data											
Seaward Kaikōura											
SKR_Main											
Jordan fw (127 m)	<b>16MFS06</b>	<b>121.91</b>	8.97	9.67	37	1.75	930	2577	5628.4	334.62	147.054
Jordan hw (219 m)	<b>13MF11</b>	<b>9.78</b>	1.68	2.03	38	1.84	117	31.19	111.5	247.62	47.8331
Jordan hw (2,494 m)	<b>15MAN06</b>	<b>45.78</b>	5.49	6.24	27	1.64	269	25.67	94.3	301.44	195.7
Apatite fission track length data											
Location	Sample ID	No. of tracks	Mean track length (um)	Standard error (um)	Standard deviation(um)	Mean Dpar (um)					
Jordan fw (127 m)	<b>16MFS06</b>	98	<b>12.22</b>	0.14	1.41	2					
Jordan hw (219 m)	<b>13MF11</b>	76	<b>13.62</b>	0.18	1.6	2.16					
Jordan hw (2,494 m)	<b>15MAN06</b>	43	<b>14.07</b>	0.15	0.96	1.87					

Note. fw = foot wall; hw = hanging wall. Primary zeta = 12.36.

## 4.1. Inland Kaikōura Mountains

### 4.1.1. IKR\_Main Transect

Within the IKR, most of the AHe analyses are reset. Ages range from ~10 to ~2 Ma from the highest (2,601 m) to lowest (278 m) elevations, with an ~7 Ma age on either side of the Clarence Fault (Table 2 and Figure S2 in the supporting information). The exception is 15TAP05AB, which was sampled from the Neogene Waima Formation (Mnw) rather than Cretaceous rocks. This sample, which sits midway up the transect at an elevation of 890 m directly adjacent to the Clarence Fault in the foot wall, has an unreset mean age of 27.5 ( $\pm 1.0$ ) Ma, indicating that it was buried less than 1 to 2 km since its deposition in the early Miocene (Browne, 1995). Only a sliver of Neogene Mnw remains in the modern Clarence Valley, all located close to the Clarence Fault, in the foot wall (Figure 2, orange unit). Map patterns indicate that this unit was more widespread in the past having been removed to expose the underlying Torlesse greywacke during deformation and development of the Kaikōura Ranges. Preservation of such a thin deposit of Wnw along the Clarence Fault, with more deeply exhumed Torlesse above and below, is a bit puzzling. One possible reason for preservation of the Wnw unit relates to its position on the mountain flank relative to the Clarence River, which is likely the primary agent of erosion in the valley. The thin deposit sits in the fault foot wall, 600 m up the hillside away from the incising Clarence River (Figure 2).

The ZHe results show a pattern of some reset ZHe ages in the hanging wall and no reset ages in the foot wall (Figure 3). For example, ZHe data from the lowest elevation hanging wall sample above the Clarence Fault (996 m) are reset and yield ages from ~32 to 46 Ma (15TAP04; Table 3), while ZHe results from a similar elevation within the opposite foot wall block (15TAP06–07; Figure 5) are unreset with ages from ~124 to 243 Ma (Table 3). The highest site in the range at 2,811 m, just below the Tapuae-o-Uenuku summit (15TAP08), yields a mean ZHe age of 109 ( $\pm 0.8$ ) Ma, which likely records the initial cooling and crystallization of the Tapuae-o-Uenuku pluton (Baker & Seward, 1996). An additional ZHe sample along the elevation transect at 2,046 m (15TAP01) has a mean age of 71.5 ( $\pm 3.4$ ) Ma (Table 3) and may be partially reset.

### 4.1.2. IKR\_Elliot Transect

Samples adjacent to the Elliot Fault, ~40 km along strike to the SW of the IKR\_Main transect (Figures 2 and S3), show trends similar to those of the IKR\_Main transect. At this site, the mean hanging wall AHe age of 3.8 ( $\pm 1.2$ ) Ma is younger than the mean foot wall age of 7.8 ( $\pm 3.3$ ) Ma.

## 4.2. Seaward Kaikōura Mountains

### 4.2.1. SKR\_Main and Mount Fyffe Transects

All AHe samples analyzed within the SKR and Amuri Ranges yield Pliocene and younger mean ages that range from ~2 to 4 Ma (Table 2 and Figure S10). The one exception is sample 14MAN04 at 698 m along the SKR\_Main profile, which has highly scattered individual grain ages that range from 1.5 to 47 Ma. Due to its poor reproducibility and anomalously old mean age, possibly due to U-Th microinclusions, we consider this sample an uninterpretable outlier and exclude it from the age-elevation plot. Other AHe ages along the SKR\_Main transect show a steep age versus elevation relationship with mean ages of ~2–3 Ma over an elevation range of ~2,400 m. Across the Jordan Thrust, the foot wall samples are older, but still Pliocene, at ~4 Ma (Figure 4 and Table 2).

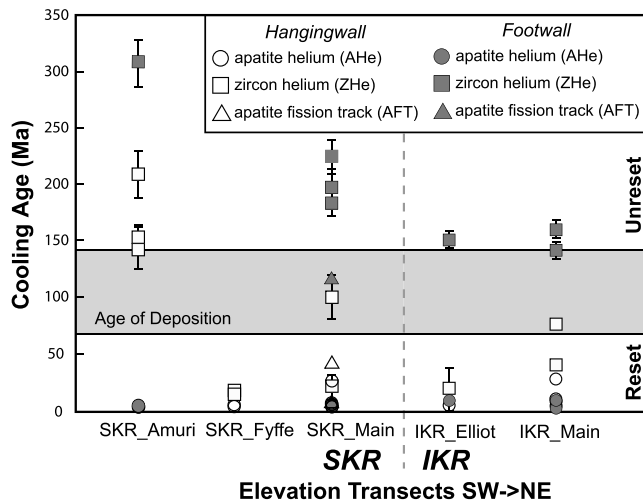


**Figure 3.** Plot of thermochronology cooling ages (apatite helium—circle symbol; zircon helium—square symbol; apatite fission track—triangle symbol) along each elevation transect site. Vertical error bars represent  $2\sigma$  standard error of mean age based on single-grain replicate ages from each sample. No error bars shown if smaller than symbol. Gray-shaded region covers the range in depositional age of sampled rocks (Torlesse (Pahua), Split Rock, and Bluff Sandstone) from GNS 1:250000 geologic map 13 and supporting text (Rattenbury et al., 2006). White symbols denote hanging wall samples and black/gray symbols denote foot wall sample sites.

A subset of three samples in the SKR was analyzed for AFT ages and lengths: two samples from the hanging wall of the Jordan Thrust (15MAN06—2,494 m at the top of the range and 13MF11—219 m adjacent to the fault) and one foot wall sample (16MFS06—127 m, ~2 km to the northeast of the SKR\_Main transect). AFT ages are 45.8 ( $\pm 6$ ) Ma and 9.8 ( $\pm 2$ ) Ma, for the high and low hanging wall samples respectively, with an older age of 122 ( $\pm 10$ ) Ma for the foot wall sample (Table 4).

Zircons from a subset of the low-elevation, hanging wall SKR samples yield mean reset ages of ~15–20 Ma (Table 3 and Figure S10). Adjacent samples at similar elevations from the foot wall yield unreset ZHe ages from ~120 to 243 Ma, similar to the AFT data pattern. An additional foot wall sample (16MFS02) located closer to the coast at <100 m also yields an unreset ZHe age of ~225 Ma. The highest site in the range (15MAN06) yields a potentially partially reset ZHe sample with replicate ages of ~82–143 Ma. Overall, the large difference in cooling ages between the relatively young hanging wall and older unreset foot wall samples (Figures 3 and 4) indicates a greater degree of hanging wall versus foot wall exhumation.

#### 4.2.2. SKR\_Amuri Transect

Samples along the SKR\_Amuri transect (Figure 2), ~30 km along strike of the Hope Fault to the southwest of Mount Manakau, all record late Cenozoic AHe ages that range from ~2 to 7 Ma (Table 2 and Figure S19). Mean AHe ages from hanging wall samples vary from 2.6 to 6.8 over 640 m of elevation. Across the Hope Fault, a sample in the foot wall has a mean age of 1.9 ( $\pm 0.6$ ) Ma, which is younger than the 2.6 ( $\pm 1.0$ ) Ma age from the nearby sample at a similar elevation in the hanging wall (Table 2), though the ages overlap with uncertainty. ZHe cooling ages from this site are Cretaceous or older in both the HW and FW, with individual grains ranging from 87 to 318 Ma (Table 3).

#### 4.3. Thermal Modeling

To first approximation, spatial trends in the reset versus nonreset thermochronology ages are interpretable without modeling, showing a pattern consistent with deeper and older exhumation in hanging wall blocks in both the IKR and SKR and widespread exhumation, including in fault foot walls, by Pliocene time. However, in order to refine time-temperature histories and constrain rates of cooling through time, we use QTQt (v.

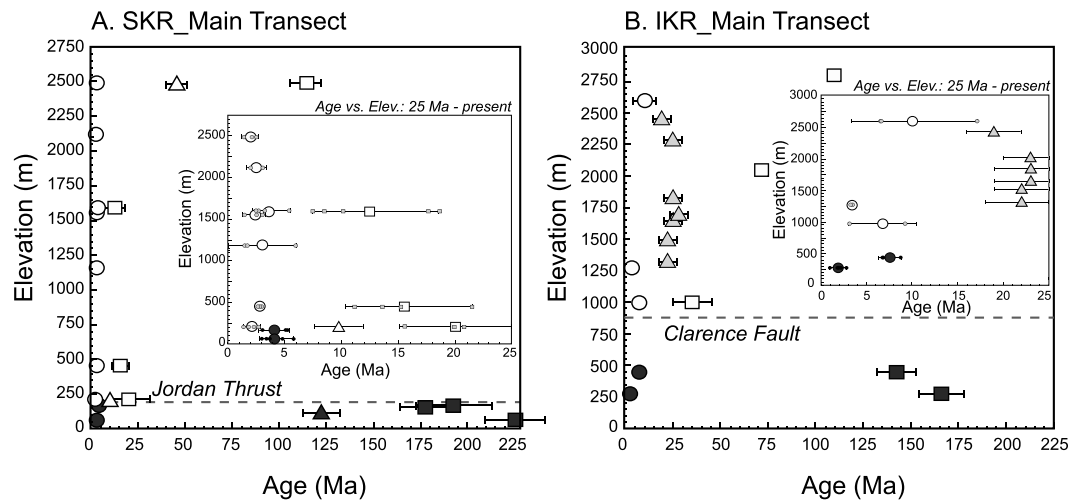


**Figure 4.** Thermochronology age-elevation plots. (a) Age-elevation data seaward Kaikōura Range (main SKR transect + two samples from neighboring Fyffe block). (b) Age-elevation data Inland Kaikōura Range main transect. Symbols and uncertainty same as in Figures 3. Gray triangles are the apatite fission track data of Baker and Seward (1996). Dashed lines show elevation of Jordan and Clarence Faults. Insets show detailed age versus elevation plot for 25 to 0 Ma (Kaikōura orogeny), including individual replicate ages (smaller symbols) as well as the mean age for helium data.

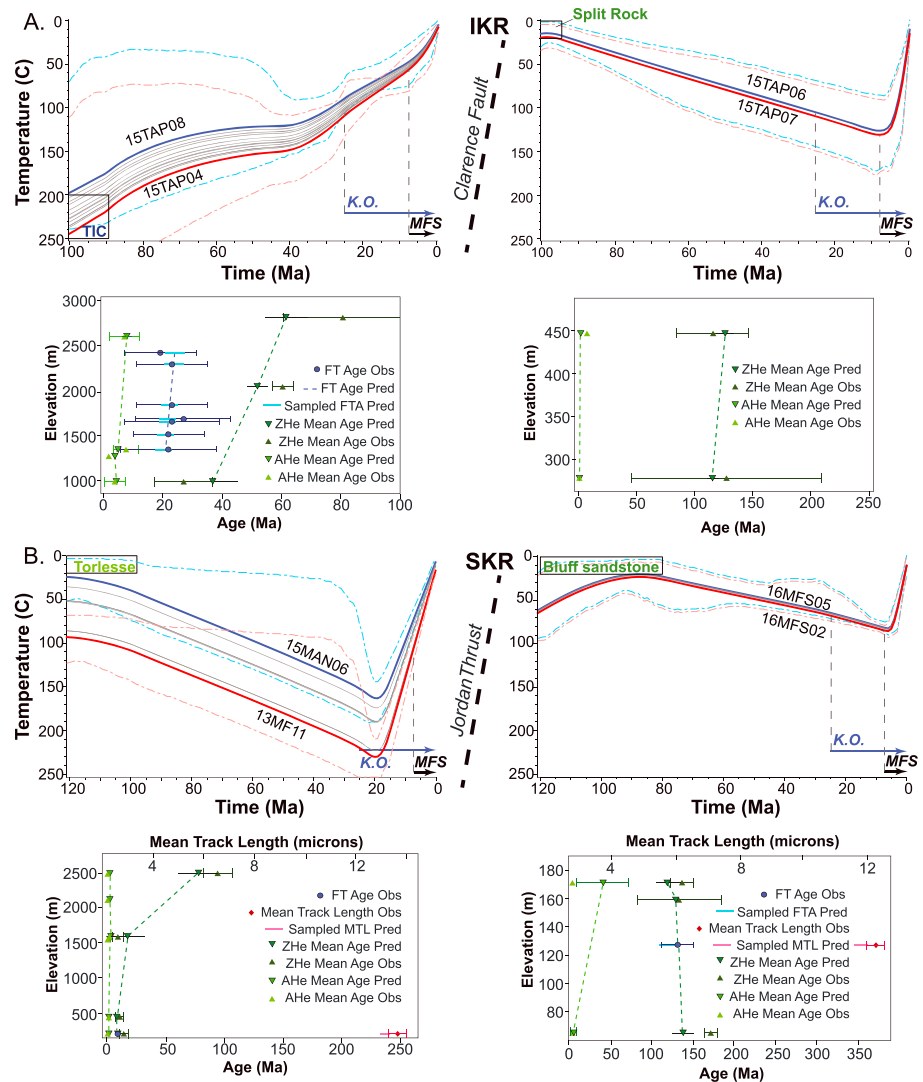


**Figure 5.** Thermal histories from QTQt inverse model results. (a–c) Time (Ma) versus temperature ( $^{\circ}\text{C}$ ) profiles from expected inverse model results. Hanging wall samples modeled as elevation profiles (left panels) and low-elevation samples or sample suites in foot wall blocks (right panel) for the Clarence (IKR), Jordan (SKR), and Hope Faults (Amuri). In cases of multiple samples along a profile, the uppermost sample thermal history plotted in blue and lowermost sample thermal history plotted in red, with the thermal histories for all samples in between shown in gray. The 95% credible intervals are drawn in cyan and magenta for the upper and lower samples, respectively. The 95% credible intervals reflect the combined uncertainty in the inferred thermal history and also the offset parameters (Gallagher, 2012). Black boxes show either the deposition or emplacement age of a sample used to constrain the model. All models included at least two thermochronometers—see text and supporting information for model input details. The blue arrow and dashed vertical lines reference the time interval of the Kaikōura Orogeny (K.O.), thought to have initiated in this part of the New Zealand plate boundary around 25 Ma. The black arrow and dashed vertical lines reference the onset of widespread dextral faulting in the Marlborough Fault System (MFS) in the late stage of orogeny beginning  $\sim 8$ –5 Ma. Lower panels are summary plots of model age predictions (pred) and the actual observed (obs) data (x axis) as a function of elevation (y axis). Error bars are included on the observed values for each data type, if available. The range in predicted values is shown as a bar across the mean predicted age. This range summarizes the mean and 95% credible range for the predictions from all thermal history models accepted during the post burn-in MCMC sampling. For AHe data, QTQt adds a small perturbation to the elevation to aid visual discrimination of data points on the plot. TIC = Tapuae-o-Uenuku igneous complex.

5.7.0R) thermal modeling software (Gallagher, 2012). The code inverts age data for time-temperature paths using a Bayesian transdimensional Markov Chain Monte Carlo method and allows us to model suites of samples along elevation profiles (Figure 4) as well as individual samples within fault foot walls.

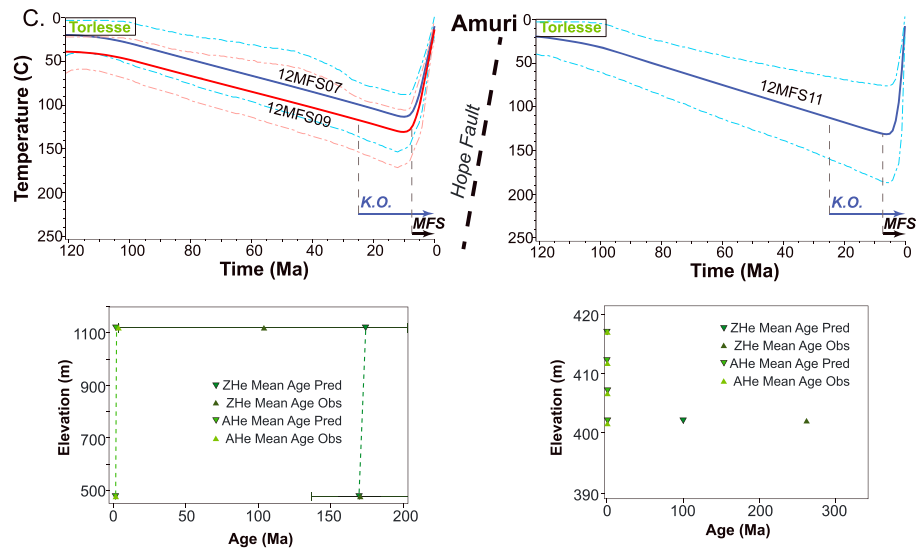


Figure 5. (continued)

We modeled AHe, ZHe, and AFT ages and track lengths, depending on the data available for each modeled sample (see supporting information for detailed model inputs). Model inputs included raw age and uncertainty,  $eU$  (effective Uranium), and crystal geometry of individual grains for helium samples and count and length data for fission track samples. AFT densities and  $c$  axis-projected track length distributions were modeled using a modification of the fanning Arrhenius model (Ketcham et al., 2007, 2009), and AHe and ZHe data were modeled with diffusion properties of Flowers et al. (2009) and Guenther et al. (2013), respectively. Model runs were set up with thermal history parameters that included ranges in time and temperature general priors as well as a range in potential surface temperatures. When modeling multiple samples along a profile, we also specified a range in present day and past temperature gradient that was allowed to vary over time. Models were further constrained by the stratigraphic or emplacement age of samples. Models were run until the chains converged (i.e., no obvious trend in the likelihood/posterior chains), which occurred, in most cases, after 100,000 post-burn-in iterations. The output of the model that we interpret (the “expected model”) is an ensemble of thermal histories, which quantifies the range of accepted models in terms of a (posterior) probability distribution (Gallagher, 2012).

#### 4.3.1. IKR

Thermal models of the IKR\_Main transect, within the hanging wall of the Clarence Fault, included a total of 12 samples (11 mafic igneous rocks and 1 Torlesse sandstone—the lowest sample in the profile) spanning 1,815 m of elevation. We exclude the unreset AHe Waima Formation sample from this analysis because it has a different thermal history from the rest of the rocks on the transect. In addition to six new AHe and ZHe data from this study, the model also included seven published AFT ages (Baker & Seward, 1996) from neighboring sample sites on the NW side of the peak (Figure S1 and Table S1). Model inversion results reveal two cooling events from the mid-Cretaceous to present (red and blue lines Figure 5a, left panel). First, there is a broad cooling of  $\sim 2$  °C/Ma from 100 to  $\sim 60$  Ma that we relate to cooling after emplacement of the Tapuae-o-Uenuku Igneous Complex at  $\sim 100$  Ma (Baker & Seward, 1996). A second, slightly faster cooling interval initiated between 35 and 40 Ma and continued to present at rates of  $\sim 3$ – $4$  °C/Ma. We relate this second event to exhumation driven by faulting and uplift during the Kaikōura orogeny.

Most estimates for the timing of initiation of uplift and erosion associated with orogeny in this part of New Zealand are closer to 25 Ma. The older initiation of cooling in the model could reflect early deformation along the Clarence Fault associated with the very beginning stages of AUS-PAC plate collision. However, 95% credible intervals on the highest and lowest samples in the profile (cyan and magenta dashed lines, Figure 5a) permit a more complicated thermal history, with spikes of faster cooling/exhumation between 25 and 30 Ma and between 5 and 10 Ma, which better matches timing of tectonic intervals from existing geologic data. A period of relative stasis within the 130 to 150 °C temperature window (for the top sample) between 60 and 40 Ma represents an interval of no exhumation or possibly deposition and burial during that time.

**Table 5**  
*Cenozoic Cooling Intervals and Apparent Exhumation Rates*

Model name	Cooling interval <sup>a</sup>	Total cooling <sup>a</sup>	Cooling rate	Thermal gradient <sup>b</sup>	Apparent exhumation rate
IKR_Main	35 to 0 Ma	110–130 °C	3–4 °C/Ma	20 °C/km	0.2 mm/year
IKR_footwall	5 to 0 Ma	110 °C	22 °C/Ma	26 °C/km	0.8 mm/year
SKR_Main	19 to 0 Ma	155–212 °C	8–11 °C/Ma	30 °C/km	0.3–0.4 mm/year
SKR_footwall	5 to 0 Ma	70 °C	14 °C/Ma	30 °C/km	0.5 mm/year
Amuri_hanging_wall	8 to 0 Ma	100–115 °C	12–14 °C/Ma	27 °C/km	0.4–0.5 mm/year
Amuri_footwall	4 to 0 Ma	125 °C	31 °C/Ma	25 °C/km	1.2 mm/year

<sup>a</sup>Estimated from QTQt thermal history plot. <sup>b</sup>Temperature gradient average from QTQt expected model.

We modeled AHe and ZHe data from two sedimentary samples (Split Rock and Torlesse Formations) along the lower flanks of the IKR, within the Clarence Fault foot wall. The thermal history results show heating that we associate with burial from the time of deposition at ~100 Ma until a switch to rapid cooling at rates of ~20 °C/Ma that we associate with exhumation from 5 Ma to present (Figure 5a, right panel).

#### 4.3.2. SKR

Models of the SKR\_Main transect, within the hanging wall of the Jordan Thrust, included a total of six Torlesse samples (including up to three chronometers, AHe, ZHe, and AFT, per sample) spanning 2,275 m of elevation. Results show heating from the time of Torlesse deposition at ~120 Ma that we associate with burial until a switch to cooling at rates of ~8–11 °C/Ma from exhumation beginning at ~19 Ma (Figure 5b, left panel). Four samples—one Split Rock Formation and three Torlesse Formation (including up to three chronometers, AHe, ZHe, and AFT, per sample)—were modeled within the Jordan Thrust foot wall. The thermal model from an inversion of these samples shows heating from the time of deposition at ~90 Ma until a switch to rapid cooling at rates of ~15 °C/Ma from 5 to 4 Ma to present (Figure 5b, right panel), again associated with a period of burial followed by exhumation.

#### 4.3.3. Hope Fault/Amuri Range

We modeled AHe and ZHe data from two sedimentary samples (Torlesse Formation) in the Amuri Range, within the hanging wall of the Hope Fault. The model shows heating presumably from burial after the time of Torlesse deposition at ~120 Ma until a switch to rapid cooling at rates of ~14 °C/Ma starting at 8 to 5 Ma and continuing to present (Figure 5c, left panel). In the foot wall, we model AHe and ZHe data of an individual Torlesse sample collected just south of Hope Fault (Figures 2 and S19). The model shows heating from the time of Torlesse deposition at ~120 Ma until a switch to very rapid cooling at rates of ~30 °C/Ma from 4 to 3 Ma to present (Figure 5c, right panel), though there is a high degree of uncertainty on this estimate given that the model is derived from only a single sample (see credible interval bounds in Figure 5c).

#### 4.3.4. Thermal Modeling Summary

Thermal modeling results confirm differences in cooling histories in hanging wall versus foot wall samples along the Clarence, Jordan, and Hope Faults. At all three sites, cooling that we associate with exhumation occurs earlier in the hanging wall than in the foot wall and we see a spatial progression in onset of the timing of exhumation from north to south (Figure 5). We find a first phase of Neogene cooling that may have begun as early as 35–40 Ma in the IKR, at around 19 Ma in the SKR, and at 8–5 Ma in the Amuri Range. At all three sites, foot wall exhumation began at or after 5 Ma.

Using the modeled t-T paths and thermal gradients (from modeled offset temperatures along profiles), we approximate rates of exhumation (Table 5) for each of the Cenozoic cooling events in the modeled thermal histories (Figure 5). We consider these to be apparent exhumation rates as we have not accounted for potential heat advection in response to erosion or perturbations of the thermal field by topography, and the rates are calculated over different time intervals. With these caveats in mind, apparent rates of exhumation vary among locations (from 0.2 to 1.2 mm/year), but to first order, we find faster cooling and apparent exhumation rates in the foot wall blocks than in hanging walls and at locations close to either the Clarence River or the Pacific Coast.

## 5. Discussion

Cooling histories from low-temperature thermochronology of the IKR and SKR provide insight into transpressive Marlborough Fault deformation related to the oblique PAC-AUS collision over the past ~25 Ma



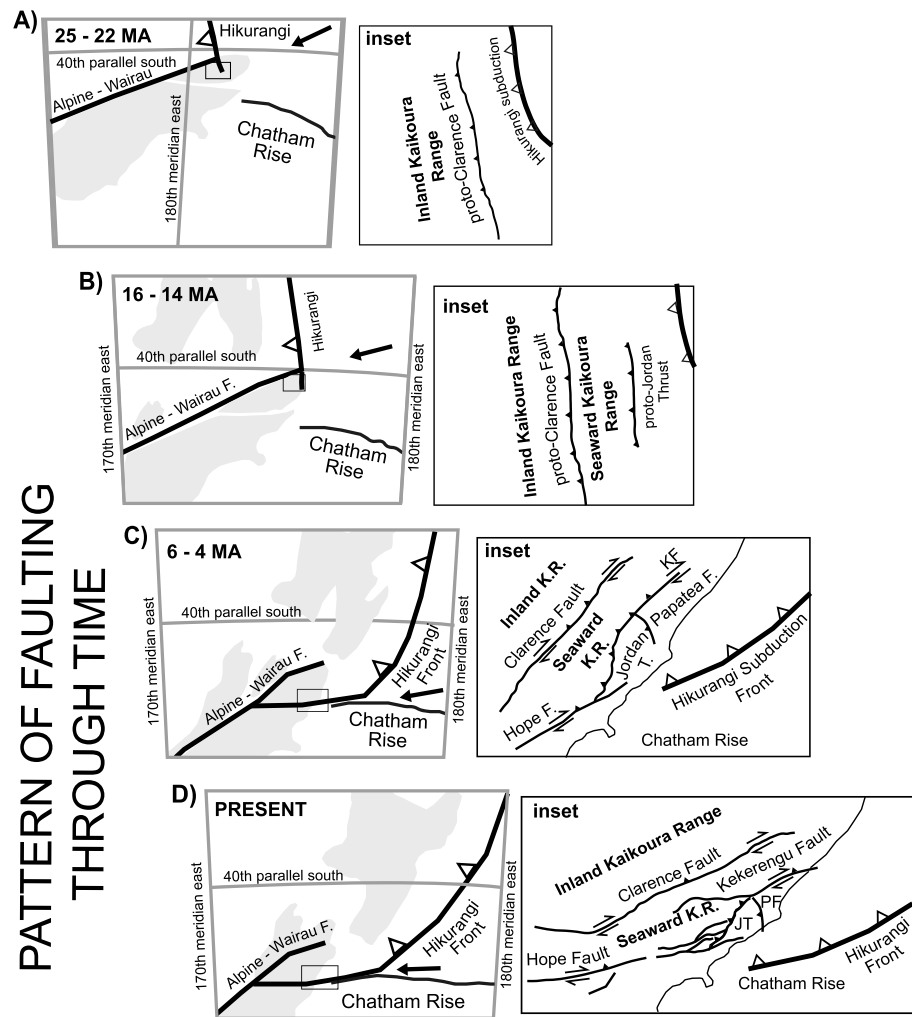


**Figure 6.** Schematic cartoon of potential Inland and Seaward Kaikōura Range and fault development through time in the context of the rotating and southward migrating Hikurangi subduction margin. Figure adapted from Jiao et al. (2017), with tectonic reconstruction after King (2000), relative plate motions interpolated from Cande and Stock (2004), and rotation of eastern North Island relative to the Australian Plate simplified from Lamb (2011). Note that our data set does not constrain timing or amounts of rotation and thus would also be consistent with the model of Little and Roberts (1997) with rotation of faults limited to NE end of the Clarence Fault. Major blocks of present-day landmass shown in gray. Insets depict fault and mountain range activity based on our thermochronology data results. Locations of structures are approximate and assumes rotation along with the Hikurangi margin (Randall et al., 2011).

(Figure 6). The data suggest that two general periods of Cenozoic exhumation occurred in the study area: a Miocene-Pliocene period of exhumation concentrated in hanging wall rocks recorded by contrasting ZHe dates across the faults followed by more widespread exhumation recorded by Pliocene and younger AHe dates across the region, in both hanging wall and foot wall samples. Below we discuss the details of these two time periods with respect to Marlborough faulting and compare exhumation histories between the IKR and SKR.

### 5.1. Onset and Early Stages of Kaikōura Orogeny

Late Eocene to mid-Miocene ZHe hanging wall ages compared to predepositional foot wall ages (Figure 3) at similar elevations across the Elliot, Clarence, and Jordan Faults indicate a greater total magnitude of exhumation in hanging walls that we relate to reverse dip-slip motion in the past (Figures 6a and 6b). The time-temperature history from Mount Tapuae-o-Uenuku shows an increase in cooling rate by 25 Ma (possibly as early as 40 Ma) that we relate to vertical motion along the Clarence Fault and uplift of the IKR, heralding the

onset of the Kaikōura orogeny (Figure 6a). Similar (U-Th/He) data from the Elliot strand along fault strike suggest that early exhumation, and by proxy faulting and mountain building, occurred along much of the length of the Clarence Fault.

Seaward Kaikōura thermochronology data provide evidence that mountain building and Jordan thrust faulting were also active in the early stages of the Kaikōura orogeny, but initiated later, at ~19 Ma (Figure 6b). In contrast to the Clarence Fault, vertical motion along the proto-Jordan Thrust appears to have been spatially limited. ZHe ages ~25 km to the SE, from the Amuri Range, in the hanging wall of the Hope Fault (Figure 2), are notably unreset, and thermal modeling suggests that exhumation did not begin here until later, at 8 to 5 Ma. A lack of Miocene cooling in the Amuri Range likely reflects a later age of initiation of faulting on the Hope Fault. It is also possible that the fault existed earlier but had an orientation less oblique to the plate motion vector than the Clarence and Jordan Faults (Little & Roberts, 1997). If early fault motion was primarily strike slip without much mountain building to trigger exhumation, then it would go undetected by our technique.

The interpretation of cooling from uplift and erosion of thrust highlands within the early collision history after a period of heating from deposition and burial, fits well with sedimentation in basins adjacent to the Kaikōura Ranges. The sedimentary record shows deposition of fine-grained marine sedimentary rocks from the late Cretaceous to the Oligocene throughout the field area (Rattenbury et al., 2006) followed by a major influx of Neogene coarser clastic sediment (Rattenbury et al., 2006), including the Miocene Great Marlborough Conglomerate (Reay, 1993). Middle-to-late Oligocene AHe ages from the Great Marlborough Conglomerate sample adjacent to the Clarence Fault (sample # 15TAP05AB) also support fast erosion from a nearby source between 30 and 25 Ma. Our data are also consistent with previous hypotheses that propose that portions of the Marlborough Faults are reactivated thrust faults from the early stages of development of the PAC-AUS plate boundary (Lamb & Bibby, 1989; Rait et al., 1991; Randall et al., 2011; Vickery & Lamb, 1995; Walcott, 1978), when at least some fault segments may have been oriented favorably with respect to the Pacific Plate motion vector to accommodate contraction (Figures 6a and 6b). We note that our data set does not constrain timing or amounts of rotation, only exhumation, so our results do not preclude the model of Little and Roberts (1997), with rotation of faults limited to NE end of the Clarence Fault.

## 5.2. Late Kaikōura Orogeny

In contrast to the higher-temperature chronometers, AHe ages are reset and all <10 Ma (most <5 Ma) across the study area. This pattern of cooling ages and thermal models suggests that exhumation was widespread across the MFS during the later stages of Kaikōura orogeny and no longer limited to Clarence and Jordan Fault hanging wall rocks (Figures 6c and 6d). We find young AHe ages on both sides of each of the faults we studied, in some cases overlapping within uncertainty. One interpretation of this pattern is that vertical slip on the segments of Marlborough Faults active early in the orogeny was greatly reduced or absent from Pliocene time onward. However, modeled time-temperature histories of hanging wall sample suites do not show a decline in cooling rates from Pliocene to present (Figure 5), which we might expect if contraction fully ceased across the faults. Consequently, we suggest that some contraction continued along these faults, even as they record predominantly strike-slip motion, and note that even if the faults rotated from orientations more conducive to thrusting in the past, their current strike is still oblique to the present-day plate motion vector (Lamb & Bibby, 1989). Moreover, there is Quaternary evidence that they accommodate oblique rather than pure dextral slip (Little & Jones, 1998; Nicol & Van Dissen, 2002; Van Dissen & Yeats, 1991). We suggest then that the lack of significant offset in AHe ages across the faults relates not to a full cessation of hanging wall uplift but rather to an increase in foot wall uplift related to other neighboring structures, which would effectively erase relative offset in AHe ages across the Clarence, Jordan, and Hope Faults.

Without more detailed geologic mapping, we cannot conclusively identify which structures specifically cause uplift and post-Pliocene rapid exhumation across the field site, but we speculate here on potential sources based on proximity of sample sites to mapped features. Rapid exhumation of Clarence foot wall samples within the Clarence Valley potentially relates to broad uplift associated with the dextral-reverse Kekerengu Fault to its south (Figure 2). Young AHe ages in the foot wall of the Jordan Thrust could relate to nearby uplift of the Papatea Block along the north striking sinistral reverse Papatea Fault (Langridge et al., 2018) or possibly faults offshore (Barnes et al., 1998), which are thought to lead to uplift of marine terraces

along the Pacific coast at 1 mm/year (Ota et al., 1995, 1996). We attribute rapid exhumation within the Amuri Range to the initiation of the Hope Fault sometime between 8 and 5 Ma. Rapid exhumation of the foot wall sample adjacent to the Hope Fault, a few million years later, may be linked to structures mapped within the transpressional North Canterbury Domain, the closest being the Stone Jug Fault. In all of these cases, we cannot rule out the possibility that uplift related to unmapped structures and/or blind faults drives exhumation at our sample sites.

What drove this proposed structural development and a change from hanging wall limited to more widespread uplift and exhumation across the MFS during the later phase of orogeny? We suggest that this change in spatial pattern relates to dextral motion of crust along the central Marlborough Faults, which likely drives deformation and crustal thickening along eastern fault terminations in the region where we find widespread young AHe ages. Little and Roberts (1997) and Walcott (1998) described such a process of seaward translation and overthrusting of crust atop the downgoing subducted slab, predicting vertical axis rotation, deformation, and some uplift as part of the process. Geophysical data lend support to this conceptual framework. Based on 3-D seismic velocity inversions, Eberhart-Phillips and Bannister (2010) found a zone of crustal thickening in the overlying plate above the subducted slab, which decreases toward the NE along strike of the Marlborough Faults. They argue for a space problem that leads to ramp-like uplift in the Kaikōura Ranges due to dextral faults translating this thicker crust into the shallow Pacific slab, which is locked at its southern end by the Chatham Rise.

In a recent publication, Jiao et al. (2017) estimate that an increase in convergence rates in eastern Marlborough took place at ~4 Ma. This is the same time period over which the Hikurangi margin and dextral motion along the main Marlborough Faults propagated southward, and the plate boundary zone widened (Holt & Haines, 1995; Knuepfer, 1992; Little & Jones, 1998; Little & Roberts, 1997), suggesting a potential relationship among these phenomena. Their model predicts a commensurate increase in exhumation rates (see their Figure 5c), which they presume would reflect the recent initiation of uplift of the SKR (Van Dissen & Yeats, 1991). A Pliocene increase in convergence rates does overlap in time with the initiation of rapid exhumation in surrounding foot wall rocks to the E-SE of both the Jordan and Clarence Faults (Figure 5b) and along the Hope Fault that we document here. However, our data record a steady, unchanging rate of exhumation in the Jordan Thrust hanging wall from ~19 Ma to present (Figure 5b), which suggests a middle Miocene rather than Pliocene Jordan Fault onset and rise of the SKR.

## 6. Conclusions

In this study, we present new low-temperature thermochronology data from the MFS and Kaikōura Ranges of New Zealand, an area of tectonic transition from Pacific Plate subduction to Alpine strike-slip faulting and Southern Alps continental collision. The data reveal two general phases of Cenozoic exhumation related to the accommodation of oblique PAC-AUS convergence during the Kaikōura Orogeny. Patterns in thermochronology ages and thermal modeling of sample suites provides evidence of vertical uplift, mountain building, and exhumation on proto-Marlborough thrust faults early in the Kaikōura orogeny. Exhumation happened first in the IKR and then in the SKR but was limited to hanging wall samples only.

Later, after late Miocene/early Pliocene onset of dextral faulting across the MFS, we find evidence of widespread, rapid exhumation at all sites, including low elevation samples in fault foot walls, and on the back-sides of the Kaikōura Ranges. We attribute continued contraction on oblique Marlborough Faults and initiation of new structures affecting fault foot walls to this pervasive Pliocene-to-present exhumation across the eastern MFS. Translation of crust along the Marlborough Faults into a subduction front locked on its southern end may have generated vertical block rotations, new fault development, and crustal thickening during this phase of orogeny.

The temporal progression in exhumation that we document here suggests that deformation migrated outward from the Inland Kaikōura Range first (40–25 Ma), then to the SKR (19 Ma), and the Amuri Range (8–5 Ma), and finally to low-elevation samples in MFS fault foot walls (Figure 6), with faster rates in the SKR and Amuri than in the IKR. We relate this spatial pattern in exhumation generally to the evolving plate boundary, including the proximity of the southward migrating edge of the Hikurangi margin through time.

## Acknowledgments

This project was made possible through generous support from the National Science Foundation (grants EAR-132859 and EAR-1321735 to Duvall, Tucker, and Flowers and EAR-1126991 to Flowers) and the National Geographic Society. Additional support from a GSA student research grant and University of Washington Department of Earth and Space Sciences graduate student grant to Collett is appreciated. Upton was supported by the New Zealand Ministry for Business Innovation and Employment (grant C05X1103). We thank Jim Metcalf at CU Boulder TRaIL lab for (U-Th-Sm)/He analyses and Paul O'Sullivan at Geosep services for apatite fission track analyses. We thank Chris Mattinson at Central Washington University and GeoSep services for help with mineral separations. We thank Diane Seward for donating apatite grains from the Tapuae-o-Uenuku sample collection for helium analysis. We gratefully acknowledge the New Zealand Department of Conservation for sampling permission. We thank Sarah Harbert, Jody Bourgeois, Jenny Knuth, Lance Colley, Deni Murray, Grant South and Hidden Valleys Raft Company, and Kaikōura Whale Watch helicopters for field and sampling assistance. We thank Alex Lechler and Sarah Harbert for constructive discussions of this work. All data from this study appear in Tables 1–5, figures in the main text, and in the supporting information tables and figures. Thermal modeling inputs are detailed in the supporting information. The paper benefited significantly from comprehensive reviews by Tim Little, an anonymous reviewer, Associate Editor Peter van der Beek, and Editor Taylor Schildgen. We greatly appreciate their detailed, constructive assessments of this work.

## References

- Albino, I., Cavazza, W., Zattin, M., Okay, A. I., Adamia, S., & Sadradze, N. (2014). Far-field tectonic effects of the Arabia–Eurasia collision and the inception of the North Anatolian Fault system. *Geological Magazine*, *151*(02), 372–379. <https://doi.org/10.1017/S0016756813000952>
- Anderson, H., Webb, T., & Jackson, J. (1993). Focal mechanisms of large earthquakes in the South Island of New Zealand: Implications for the accommodation of Pacific–Australia plate motion. *Geophysical Journal International*, *115*(3), 1032–1054. <https://doi.org/10.1111/j.1365-246X.1993.tb01508.x>
- Baker, J., & Seward, D. (1996). Timing of Cretaceous extension and Miocene compression in northeast South Island, New Zealand: Constraints from Rb–Sr and fission-track dating of an igneous pluton. *Tectonics*, *15*(5), 976–983. <https://doi.org/10.1029/96TC00626>
- Barnes, P. M., Lépinay, B. M., Collot, J. Y., Delteil, J., & Audru, J. C. (1998). Strain partitioning in the transition area between oblique subduction and continental collision, Hikurangi margin, New Zealand. *Tectonics*, *17*(4), 534–557. <https://doi.org/10.1029/98TC00974>
- Bartholomew, T. D., Little, T. A., Clark, K. J., Van Dissen, R., & Barnes, P. M. (2014). Kinematics and paleoseismology of the Vernon Fault, Marlborough Fault System, New Zealand: Implications for contractional fault bend deformation, earthquake triggering, and the record of Hikurangi subduction earthquakes. *Tectonics*, *33*, 1408–1424. <https://doi.org/10.1002/2014TC003545>
- Batt, G. E., & Braun, J. (1999). The tectonic evolution of the Southern Alps, New Zealand: Insights from fully thermally coupled dynamical modeling. *Geophysical Journal International*, *136*(2), 403–420. <https://doi.org/10.1046/j.1365-246X.1999.00730.x>
- Batt, G. E., Braun, J., Kohn, B. P., & McDougall, I. (2000). Thermochronological analysis of the dynamics of the Southern Alps, New Zealand. *Geological Society of America Bulletin*, *112*(2), 250–266. [https://doi.org/10.1130/0016-7606\(2000\)112<250:TAOTDO>2.0.CO;2](https://doi.org/10.1130/0016-7606(2000)112<250:TAOTDO>2.0.CO;2)
- Beaumont, C., Kamp, P. J., Hamilton, J., & Fullsack, P. (1996). The continental collision zone, South Island, New Zealand: Comparison of geodynamical models and observations. *Journal of Geophysical Research*, *101*(B2), 3333–3359. <https://doi.org/10.1029/95JB02401>
- Beavan, J., Moore, M., Pearson, C., Henderson, M., Parsons, B., Bourne, S., et al. (1999). Crustal deformation during 1994–1998 due to oblique continental collision in the central Southern Alps, New Zealand, and implications for seismic potential of the Alpine Fault. *Journal of Geophysical Research*, *104*(B11), 25,233–25,255. <https://doi.org/10.1029/1999JB900198>
- Benowitz, J. A., Layer, P. W., Armstrong, P., Perry, S. E., Haeussler, P. J., Fitzgerald, P. G., & VanLaningham, S. (2011). Spatial variations in focused exhumation along a continental-scale strike-slip fault: The Denali fault of the eastern Alaska Range. *Geosphere*, *7*(2), 455–467. <https://doi.org/10.1130/GES00589.1>
- Benson, A. M., Little, T. A., Van Dissen, R. J., Hill, N., & Townsend, D. B. (2001). Late Quaternary paleoseismic history and surface rupture characteristics of the eastern Awatere strike-slip fault, New Zealand. *Geological Society of America Bulletin*, *113*(8), 1079–1091. [https://doi.org/10.1130/0016-7606\(2001\)113<1079:LQPHAS>2.0.CO;2](https://doi.org/10.1130/0016-7606(2001)113<1079:LQPHAS>2.0.CO;2)
- Brothers, R. N. (1974). Kaikōura orogeny in Northland, New Zealand. *New Zealand Journal of Geology and Geophysics*, *17*(1), 1–18. <https://doi.org/10.1080/00288306.1974.10427986>
- Browne, G. H. (1992). The northeastern portion of the Clarence Fault: Tectonic implications for the late Neogene evolution of Marlborough, New Zealand. *New Zealand Journal of Geology and Geophysics*, *35*(4), 437–445. <https://doi.org/10.1080/00288306.1992.9514538>
- Browne, G. H. (1995). Sedimentation patterns during the Neogene in Marlborough, New Zealand. *Journal of the Royal Society of New Zealand*, *25*(4), 459–483. <https://doi.org/10.1080/03014223.1995.9517497>
- Cande, S. C., & Stock, J. M. (2004). Pacific–Antarctic–Australia motion and the formation of the Macquarie Plate. *Geophysical Journal International*, *157*(1), 399–414. <https://doi.org/10.1111/j.1365-246X.2004.02224.x>
- Carrapa, B., Trimble, J. D., & Stockli, D. F. (2011). Patterns and timing of exhumation and deformation in the Eastern Cordillera of NW Argentina revealed by (U–Th)/He thermochronology. *Tectonics*, *30*, TC3003. <https://doi.org/10.1029/2010TC002707>
- Clark, M. K., Farley, K. A., Zheng, D., Wang, Z., & Duvall, A. R. (2010). Early Cenozoic faulting of the northern Tibetan Plateau margin from apatite (U–Th)/He ages. *Earth and Planetary Science Letters*, *296*(1–2), 78–88. <https://doi.org/10.1016/j.epsl.2010.04.051>
- Colgan, J. P., Dumitru, T. A., Reiners, P. W., Wooden, J. L., & Miller, E. L. (2006). Cenozoic tectonic evolution of the Basin and Range Province in northwestern Nevada. *American Journal of Science*, *306*(8), 616–654. <https://doi.org/10.2475/08.2006.02>
- Cowan, H. A. (1989). *An evaluation of the Late Quaternary displacements and seismic hazard associated with the Hope and Kakapo Faults, Amuri District, North Canterbury*. MSc Thesis (Eng Geol). Christchurch: University of Canterbury.
- Davey, F. J., Henyey, T., Holbrook, W. S., Okaya, D., Stern, T. A., Melhuish, A., et al. (1998). Preliminary results from a geophysical study across a modern, continent–continent collisional plate boundary—The Southern Alps, New Zealand. *Tectonophysics*, *288*(1–4), 221–235. [https://doi.org/10.1016/S0040-1951\(97\)00297-7](https://doi.org/10.1016/S0040-1951(97)00297-7)
- Dodson, M. H. (1973). Closure temperature in cooling geochronological and petrological systems. *Contributions to Mineralogy and Petrology*, *40*(3), 259–274. <https://doi.org/10.1007/BF00373790>
- Donelick, R. A., O'Sullivan, P. B., & Ketcham, R. A. (2005). Apatite fission-track analysis. *Reviews in Mineralogy and Geochemistry*, *58*(1), 49–94. <https://doi.org/10.2138/rmg.2005.58.3>
- Duvall, A. R., Clark, M. K., Kirby, E., Farley, K. A., Craddock, W. H., Li, C., & Yuan, D. (2013). Low-temperature thermochronometry along the Kunlun and Haiyuan Faults, NE Tibetan Plateau: Evidence for kinematic change during late-stage orogenesis. *Tectonics*, *32*, 1190–1211. <https://doi.org/10.1002/tect.20072>
- Eberhart-Phillips, D., & Reyners, P. (1997). Continental subduction and three-dimensional crustal structure: The northern South Island, New Zealand. *Journal of Geophysical Research*, *102*(B6), 11,843–11,861. <https://doi.org/10.1029/96JB03555>
- Eberhart-Phillips, D., & Bannister, S. (2010). 3-D imaging of Marlborough, New Zealand, subducted plate and strike-slip fault systems. *Geophysical Journal International*, *192*, 73–96. <https://doi.org/10.1111/j.1365-246X.2010.04621.x>
- Farley, K. A. (2000). Helium diffusion from apatite: General behavior as illustrated by Durango fluorapatite. *Journal of Geophysical Research*, *105*(B2), 2903–2914. <https://doi.org/10.1029/1999JB900348>
- Fitzgerald, P. G., & Gleadow, A. J. W. (1990). New approaches in fission track geochronology as a tectonic tool: examples from the Transantarctic Mountains. *International Journal of Radiation Applications and Instrumentation. Part D. Nuclear Tracks and Radiation Measurements*, *17*(3), 351–357. [https://doi.org/10.1016/1359-0189\(90\)90057-5](https://doi.org/10.1016/1359-0189(90)90057-5)
- Fitzgerald, P. G., Sorkhabi, R. B., Redfield, T. F., & Stump, E. (1995). Uplift and denudation of the central Alaska Range: A case study in the use of apatite fission track thermochronology to determine absolute uplift parameters. *Journal of Geophysical Research*, *100*(B10), 20,175–20,191. <https://doi.org/10.1029/95JB02150>

- Flowers, R. M., Ketcham, R. A., Shuster, D. L., & Farley, K. A. (2009). Apatite (U-Th)/He thermochronometry using a radiation damage accumulation and annealing model. *Geochimica et Cosmochimica Acta*, 73(8), 2347–2365. <https://doi.org/10.1016/j.gca.2009.01.015>
- Flowers, R. M., Shuster, D. L., Wernicke, B. P., & Farley, K. A. (2007). Radiation damage control on apatite (U-Th)/He dates from the Grand Canyon region, Colorado Plateau. *Geology*, 35(5), 447–450. <https://doi.org/10.1130/G23471A.1>
- Furlong, K. P. (2007). Locating the deep extent of the plate boundary along the Alpine Fault zone, New Zealand: Implications for patterns of exhumation in the Southern Alps. *Special Papers-Geological Society of America*, 474(3-4), 449–462. <https://doi.org/10.1016/j.tecto.2009.04.023>
- Furlong, K. P., & Kamp, P. J. (2009). The lithospheric geodynamics of plate boundary transpression in New Zealand: Initiating and emplacing subduction along the Hikurangi margin, and the tectonic evolution of the Alpine Fault system. *Tectonophysics*, 474(3–4), 449–462. <https://doi.org/10.1016/j.tecto.2009.04.023>
- Galbraith, R. F., & Laslett, G. M. (1993). Statistical models for mixed fission track ages. *Nuclear Tracks and Radiation Measurements*, 21(4), 459–470. [https://doi.org/10.1016/1359-0189\(93\)90185-C](https://doi.org/10.1016/1359-0189(93)90185-C)
- Gallagher, K. (2012). Transdimensional inverse thermal history modelling for quantitative thermochronology. *Journal of Geophysical Research*, 117, B02408. <https://doi.org/10.1029/2011JB00882>
- Gallagher, K., Brown, R., & Johnson, C. (1998). Fission track analysis and its applications to geological problems. *Annual Review of Earth and Planetary Sciences*, 26(1), 519–572. <https://doi.org/10.1146/annurev.earth.26.1.519>
- Gleadow, A. J. W., & Duddy, I. R. (1981). Early Cretaceous volcanism and the early breakup history of southeastern Australia: Evidence from fission track dating of volcanoclastic sediments. In M. M. Cresswell & P. Vella (Eds.), *Gondwana five-proceedings of the fifth international Gondwana Symposium* (pp. 295–300). Rotterdam, Netherlands: Balkema.
- Guenther, W. R., Reiners, P. W., Ketcham, R. A., Nasdala, L., & Giester, G. (2013). Helium diffusion in natural zircon: Radiation damage, anisotropy, and the interpretation of zircon (U-Th)/He thermochronology. *American Journal of Science*, 313(3), 145–198. <https://doi.org/10.2475/03.2013.01>
- Hall, L. S., Lamb, S. H., & Mac Niocaill, C. (2004). Cenozoic distributed rotational deformation, South Island, New Zealand. *Tectonics*, 23, TC2002. <https://doi.org/10.1029/2002TC001421>
- Herman, F., Cox, S. C., & Kamp, P. J. J. (2009). Low-temperature thermochronology and thermokinematic modeling of deformation, exhumation, and development of topography in the central Southern Alps, New Zealand. *Tectonics*, 28, TC5011. <https://doi.org/10.1029/2008TC002367>
- Holt, W. E., & Haines, A. J. (1995). The kinematics of northern South Island, New Zealand, determined from geologic strain rates. *Journal of Geophysical Research*, 100(B9), 17,991–18,010. <https://doi.org/10.1029/95JB01059>
- Jiao, R., Herman, F., & Seward, D. (2017). Late Cenozoic exhumation model of New Zealand: Impacts from tectonics and climate. *Earth-Science Reviews*, 166, 286–298. <https://doi.org/10.1016/j.earscirev.2017.01.003>
- Kamp, P. J., & Tippett, J. M. (1993). Dynamics of Pacific plate crust in the South Island (New Zealand) zone of oblique continent-continent convergence. *Journal of Geophysical Research*, 98(B9), 16,105–16,118. <https://doi.org/10.1029/93JB01091>
- Ketcham, R. A., Carter, A., Donelick, R. A., Barbarand, J., & Hurford, A. J. (2007). Improved modeling of fission-track annealing in apatite. *American Mineralogist*, 92(5–6), 799–810. <https://doi.org/10.2138/am.2007.2281>
- Ketcham, R. A., Donelick, R. A., Balestrieri, M. L., & Zattin, M. (2009). Reproducibility of apatite fission-track length data and thermal history reconstruction. *Earth and Planetary Science Letters*, 284(3–4), 504–515. <https://doi.org/10.1016/j.epsl.2009.05.015>
- Ketcham, R. A., Gautheron, C., & Tassan-Got, L. (2011). Accounting for long alpha-particle stopping distances in (U-Th-Sm)/He geochronology: Refinement of the baseline case. *Geochimica et Cosmochimica Acta*, 75(24), 7779–7791. <https://doi.org/10.1016/j.gca.2011.10.011>
- King, P. R. (2000). Tectonic reconstructions of New Zealand: 40 Ma to the present. *New Zealand Journal of Geology and Geophysics*, 43(4), 611–638. <https://doi.org/10.1080/00288306.2000.9514913>
- Kirby, E., Reiners, P. W., Krol, M. A., Whipple, K. X., Hodges, K. V., Farley, K. A., et al. (2002). Late Cenozoic evolution of the eastern margin of the Tibetan Plateau: Inferences from 40Ar/39Ar and (U-Th)/He thermochronology. *Tectonics*, 21(1), TC1001. <https://doi.org/10.1029/2000TC001246>
- Knuepfer, P. L. K. (1984). *Tectonic geomorphology and present-day tectonics of the Alpine shear system, South Island, New Zealand*, (PhD thesis, 509 pp.). Tucson: University of Arizona.
- Knuepfer, P. L. K. (1988). Estimating ages of late Quaternary stream terraces from analysis of weathering rinds and soils. *Geological Society of America Bulletin*, 100(8), 1224–1236. [https://doi.org/10.1130/0016-7606\(1988\)100<1224:EAOLQS>2.3.CO;2](https://doi.org/10.1130/0016-7606(1988)100<1224:EAOLQS>2.3.CO;2)
- Knuepfer, P. L. K. (1992). Temporal variations in latest Quaternary slip across the Australian-Pacific plate boundary, northeastern South Island, New Zealand. *Tectonics*, 11(3), 449–464. <https://doi.org/10.1029/91TC02890>
- Koons, P. O. (1989). The topographic evolution of collisional mountain belts: A numerical look at the Southern Alps, New Zealand. *American Journal of Science*, 289(9), 1041–1069. <https://doi.org/10.2475/ajs.289.9.1041>
- Lamb, S. H. (1988). Tectonic rotations about vertical axes during the last 4 Ma in part of the New Zealand plate-boundary zone. *Journal of Structural Geology*, 10(8), 875–893. [https://doi.org/10.1016/0191-8141\(88\)90101-0](https://doi.org/10.1016/0191-8141(88)90101-0)
- Lamb, S. (2011). Cenozoic tectonic evolution of the New Zealand plate-boundary zone: A paleomagnetic perspective. *Tectonophysics*, 509(3–4), 135–164. <https://doi.org/10.1016/j.tecto.2011.06.005>
- Lamb, S. H., & Bibby, H. M. (1989). The last 25 Ma of rotational deformation in part of the New Zealand plate-boundary zone. *Journal of Structural Geology*, 11(4), 473–492. [https://doi.org/10.1016/0191-8141\(89\)90024-2](https://doi.org/10.1016/0191-8141(89)90024-2)
- Langridge, R., Campbell, J., Hill, N., Pere, V., Pope, J., Pettinga, J., et al. (2003). Paleoseismology and slip rate of the Conway Segment of the Hope Fault at Greenburn Stream, South Island, New Zealand. *Annals of Geophysics*, 46(5), 1119–1139.
- Langridge, R. M., Rowland, J., Villamor, P., Mountjoy, J., Townsend, D. B., Nissen, E., et al. (2018). Coseismic rupture and preliminary slip estimates for the Papatea Fault and its role in the 2016 Mw 7.8 Kaikōura, New Zealand, earthquake. *Bulletin of the Seismological Society of America*, 108(3B), 1596–1622. <https://doi.org/10.1785/0120170336>
- Langridge, R. M., Villamor, P., Basili, R., Almond, P., Martinez-Diaz, J. J., & Canora, C. (2010). Revised slip rates for the Alpine Fault at Inchbonnie: Implications for plate boundary kinematics of South Island, New Zealand. *Lithosphere*, 2(3), 139–152. <https://doi.org/10.1130/L88.1>
- Leloup, P. H., Arnaud, N., Lacassin, R., Kienast, J. R., Harrison, T. M., Trong, T. T., et al. (2001). New constraints on the structure, thermochronology, and timing of the Ailao Shan-Red River shear zone, SE Asia. *Journal of Geophysical Research*, 106(B4), 6683–6732. <https://doi.org/10.1029/2000JB900322>

- Lewis, D. W., Laird, M. G., & Powell, R. D. (1980). Debris flow deposits of early Miocene age, Deadman stream, Marlborough, New Zealand. *Sedimentary Geology*, 27(2), 83–118. [https://doi.org/10.1016/0037-0738\(80\)90032-9](https://doi.org/10.1016/0037-0738(80)90032-9)
- Little, T. A., Cox, S., Vry, J. K., & Batt, G. (2005). Variations in exhumation level and uplift rate along the oblique-slip Alpine Fault, central Southern Alps, New Zealand. *GSA Bulletin*, 117(5), 707–723. <https://doi.org/10.1130/B25500.1>
- Little, T. A., Grapes, R., & Berger, G. W. (1998). Late Quaternary strike slip on the eastern part of the Awatere fault, South Island, New Zealand. *Geological Society of America Bulletin*, 110(2), 0127–0148. [https://doi.org/10.1130/0016-7606\(1998\)110<0127:LQSSOT>2.3.CO;2](https://doi.org/10.1130/0016-7606(1998)110<0127:LQSSOT>2.3.CO;2)
- Little, T. A., Holcombe, R. J., & Ilg, B. R. (2002). Kinematics of oblique collision and ramping inferred from microstructures and strain in middle crustal rocks, central Southern Alps, New Zealand. *Journal of Structural Geology*, 24(1), 219–239. [https://doi.org/10.1016/S0191-8141\(01\)00060-8](https://doi.org/10.1016/S0191-8141(01)00060-8)
- Little, T. A., & Jones, A. (1998). Seven million years of strike-slip and related off-fault deformation, northeastern Marlborough fault system, South Island, New Zealand. *Tectonics*, 17(2), 285–302. <https://doi.org/10.1029/97TC03148>
- Little, T. A., & Roberts, A. P. (1997). Distribution and mechanism of Neogene to present-day vertical axis rotations, Pacific-Australian plate boundary zone, South Island, New Zealand. *Journal of Geophysical Research*, 102(B9), 20,447–20,468. <https://doi.org/10.1029/97JB01279>
- Little, T. A., Van Dissen, R., Kearse, J., Norton, K., Benson, A., & Wang, N. (2018). Kekerengu fault, New Zealand: Timing and size of Late Holocene surface ruptures. *Bulletin of the Seismological Society of America*, 108(3B), 1556–1572. <https://doi.org/10.1785/0120170152>
- Mason, D. P. M., Little, T. A., & Van Dissen, R. J. (2006). Rates of active faulting during late Quaternary fluvial terrace formation at Saxon River, Awatere fault, New Zealand. *Geological Society of America Bulletin*, 118(11–12), 1431–1446. <https://doi.org/10.1130/B25961.1>
- Mazengarb, C., Begg, J. G., & Simes, J. E. (1993). Does the Esk Head Subterranean cross Cook Strait (abstract). *Misc. Pub. Geol. Soc. of New Zeal.* 79A, 113.
- McCalpin, J. P. (1996). Tectonic geomorphology and Holocene paleoseismicity of the Molesworth section of the Awatere Fault, South Island, New Zealand. *New Zealand Journal of Geology and Geophysics*, 39(1), 33–50. <https://doi.org/10.1080/00288306.1996.9514693>
- Metcalfe, J. R., Fitzgerald, P. G., Baldwin, S. L., & Munoz, J. (2009). Thermochronology of a convergent orogeny: Constraints on the timing of thrust faulting and subsequent exhumation of the Maldeta Pluton in the Central Pyrenean Axial Zone. *Earth and Planetary Science Letters*, 287(3–4), 488–503. <https://doi.org/10.1016/j.epsl.2009.08.036>
- Murray, K. E., Orme, D. A., & Reiners, P. W. (2014). Effects of U–Th-rich grain boundary phases on apatite helium ages. *Chemical Geology*, 390, 135–151. <https://doi.org/10.1016/j.chemgeo.2014.09.023>
- Nicol, A., & Van Dissen, R. (2002). Up-dip partitioning of displacement components on the oblique-slip Clarence Fault. *New Zealand Journal of Structural Geology*, 24(9), 1521–1535. [https://doi.org/10.1016/S0191-8141\(01\)00141-9](https://doi.org/10.1016/S0191-8141(01)00141-9)
- Norris, R. J., Koons, P. O., & Cooper, A. F. (1990). The obliquely-convergent plate boundary in the South Island of New Zealand: Implications for ancient collision zones. *Journal of Structural Geology*, 12(5–6), 715–725. [https://doi.org/10.1016/0191-8141\(90\)90084-C](https://doi.org/10.1016/0191-8141(90)90084-C)
- Ota, Y., Brown, L. J., Berryman, K. R., Fujimori, T., Miyauchi, T., Beu, A. G., et al. (1995). Vertical tectonic movement in northeastern Marlborough: Stratigraphic, radiocarbon, and paleoecological data from Holocene estuaries. *New Zealand Journal of Geology and Geophysics*, 38(3), 269–282. <https://doi.org/10.1080/00288306.1995.9514656>
- Ota, Y., Pillians, B., Berryman, K., Beu, A., Fujimori, T., Miyauchi, T., et al. (1996). Pleistocene coastal terraces of Kaikōura Peninsula and the Marlborough coast, South Island, New Zealand. *New Zealand Journal of Geology and Geophysics*, 39(1), 51–73. <https://doi.org/10.1080/00288306.1996.9514694>
- Rait, G., Chanier, F., & Waters, D. W. (1991). Landward- and seaward- directed thrusting accompanying the onset of subduction beneath New Zealand. *Geology*, 19(3), 230–233. [https://doi.org/10.1130/0091-7613\(1991\)019<0230:LASDTA>2.3.CO;2](https://doi.org/10.1130/0091-7613(1991)019<0230:LASDTA>2.3.CO;2)
- Randall, K., Lamb, S., & Mac Niocaill, C. (2011). Large tectonic rotations in a wide zone of Neogene distributed dextral shear, northeastern South Island, New Zealand. *Tectonophysics*, 509(3–4), 165–180. <https://doi.org/10.1016/j.tecto.2011.05.006>
- Rattenbury, M. S., Townsend, D. B., & Johnston, M. R. (compilers). (2006). Geology of the Kaikōura Area, Institute of Geological and Nuclear Sciences 1:250000 Geological Map 13, Lower Hutt, New Zealand, GNS Science, 1 sheet + 70 p.
- Reay, M. B. (1993). Geology of the middle Clarence valley. *Inst. Of Geol. and Nuc. Sci. geol. map 10*, Lower Hutt, Institute of Geol. and Nuc. Sci., 144 p. +1 map
- Reiners, P. W., & Farley, K. A. (2001). Influence of crystal size on apatite (U–Th)/He thermochronology: An example from the Bighorn Mountains, Wyoming. *Earth and Planetary Science Letters*, 188(3–4), 413–420. [https://doi.org/10.1016/S0012-821X\(01\)00341-7](https://doi.org/10.1016/S0012-821X(01)00341-7)
- Reiners, P. W., Farley, K. A., & Hicke, H. J. (2002). He diffusion and (U–Th)/He thermochronometry of zircon: Initial results from Fish Canyon Tuff and Gold Butte. *Tectonophysics*, 349(1–4), 297–308. [https://doi.org/10.1016/S0040-1951\(02\)00058-6](https://doi.org/10.1016/S0040-1951(02)00058-6)
- Reiners, P. W., Spell, T. L., Nicolescu, S., & Zanetti, K. A. (2004). Zircon (U–Th)/He thermochronometry: He diffusion and comparisons with <sup>40</sup>Ar/<sup>39</sup>Ar dating. *Geochimica et Cosmochimica Acta*, 68(8), 1857–1887. <https://doi.org/10.1016/j.gca.2003.10.021>
- Reiners, P. W., Zhou, Z., Ehlers, T. A., Xu, C., Brandon, M. T., & Donelick, R. A. (2003). Post-Orogenic evolution of the Dabie Shan, eastern China, from (U–Th)/He and fission-track thermochronology. *American Journal of Science*, 303(6), 489–518. <https://doi.org/10.2475/ajs.303.6.489>
- Ross, S. M. (2003). *Pierce's criterion for the elimination of suspect experimental data*, Ph.D. thesis, J. of Eng. Tech. (pp. 1–12). CT: University of New Haven.
- Shuster, D. L., Flowers, R. M., & Farley, K. A. (2006). The influence of natural radiation damage on helium diffusion kinetics in apatite. *Earth and Planetary Science Letters*, 249(3–4), 148–161. <https://doi.org/10.1016/j.epsl.2006.07.028>
- Spiegel, C., Kohn, B., Belton, D., Berner, Z., & Gleadow, A. (2009). Apatite (U–Th–Sm)/He thermochronology of rapidly cooled samples: The effect of He implantation. *Earth and Planetary Science Letters*, 285(1–2), 105–114. <https://doi.org/10.1016/j.epsl.2009.05.045>
- Spotila, J. A., Farley, K. A., & Sieh, K. (1998). Uplift and erosion of the San Bernardino Mountains associated with transpression along the San Andreas fault, California, as constrained by radiogenic helium thermochronometry. *Tectonics*, 17(3), 360–378. <https://doi.org/10.1029/98TC00378>
- Spotila, J. A., Farley, K. A., Yule, J. D., & Reiners, P. W. (2001). Near-field transpressive deformation along the San Andreas fault zone in southern California based on exhumation constrained by (U–Th)/He dating. *Journal of Geophysical Research*, 106(B12), 30,909–30,922. <https://doi.org/10.1029/2001JB000348>
- Sutherland, R., Davey, F., & Beavan, J. (2000). Plate boundary deformation in South Island, New Zealand, is related to inherited lithospheric structure. *Earth and Planetary Science Letters*, 177(3–4), 141–151. [https://doi.org/10.1016/S0012-821X\(00\)00043-1](https://doi.org/10.1016/S0012-821X(00)00043-1)
- Upton, P., Koons, P. O., Craw, D., Henderson, C. M., & Enlow, R. (2009). Along-strike differences in the Southern Alps of New Zealand: Consequences of inherited variation in rheology. *Tectonics*, 28, TC2007. <https://doi.org/10.1029/2008TC002353>
- Van Dissen, R., & Yeats, R. S. (1991). Hope fault, Jordan thrust, and uplift of the Seaward Kaikōura Range, New Zealand. *Geology*, 19(4), 393–396. [https://doi.org/10.1130/0091-7613\(1991\)019<0393:HFJTAU>2.3.CO;2](https://doi.org/10.1130/0091-7613(1991)019<0393:HFJTAU>2.3.CO;2)

- Vickery, S., & Lamb, S. (1995). Large tectonic rotations since the Early Miocene in a convergent plate boundary zone, South Island, New Zealand. *Earth and Planetary Science Letters*, *136*, 44–59.
- Wagner, G. A., & Reimer, G. M. (1972). Fission track tectonics: The tectonic interpretation of fission track apatite ages. *Earth and Planetary Science Letters*, *14*(2), 263–268. [https://doi.org/10.1016/0012-821X\(72\)90018-0](https://doi.org/10.1016/0012-821X(72)90018-0)
- Walcott, R. I. (1978). Present tectonics and late Cenozoic evolution of New Zealand. *Geophysical Journal of Royal Astronomical Society*, *52*(1), 137–164. <https://doi.org/10.1111/j.1365-246X.1978.tb04225.x>
- Walcott, R. I. (1998). Modes of oblique compression: Late Cenozoic tectonics of the South Island of New Zealand. *Reviews of Geophysics*, *36*(1), 1–26. <https://doi.org/10.1029/97RG03084>
- Wallace, L. M., Beavan, J., McCaffrey, R., Berryman, K., & Denys, P. (2007). Balancing the plate motion budget in the South Island, New Zealand using GPD, geological and seismological data. *Geophysical Journal International*, *168*(1), 332–352. <https://doi.org/10.1111/j.1365-246X.2006.03183.x>
- Wolf, R. A., Farley, K. A., & Silver, L. T. (1996). Helium diffusion and low-temperature thermochronometry of apatite. *Geochimica et Cosmochimica Acta*, *60*(21), 4231–4240. [https://doi.org/10.1016/S0016-7037\(96\)00192-5](https://doi.org/10.1016/S0016-7037(96)00192-5)
- Wood, R. A., Pettinga, J. R., Bannister, S., Lamarche, G., & McMorrison, T. J. (1994). Structure of the Hanmer strike-slip basin, Hope fault, New Zealand. *Geological Society of America Bulletin*, *106*(11), 1459–1473. [https://doi.org/10.1130/0016-7606\(1994\)106<1459:SOTHSS>2.3.CO;2](https://doi.org/10.1130/0016-7606(1994)106<1459:SOTHSS>2.3.CO;2)

### References From the Supporting Information

- Baker, I. A., Gamble, J. A., & Graham, I. J. (1994). The age, geology, and geochemistry of the Tapuaenuku Igneous Complex, Marlborough, New Zealand. *New Zealand Journal of Geology and Geophysics*, *37*(3), 249–268. <https://doi.org/10.1080/00288306.1994.9514620>
- Ehlers, T. A., & Farley, K. A. (2003). Apatite (U-Th)/He thermochronometry: Methods and applications to problems in tectonic and surface processes. *Earth and Planetary Science Letters*, *Frontiers*, *206*(1–2), 1–14. [https://doi.org/10.1016/S0012-821X\(02\)01069-5](https://doi.org/10.1016/S0012-821X(02)01069-5)
- Flowers, R. M., Farley, K. A., & Ketcham, R. A. (2015). A reporting protocol for thermochronologic modeling illustrated with data from the grand canyon. *Earth and Planetary Science Letters*, *432*, 425–435. <https://doi.org/10.1016/j.epsl.2015.09.053>
- MacKinnon, T. C. (1983). Origin of the Torlesse terrane and coeval rocks, South Island, New Zealand. *Geological Society of America Bulletin*, *94*(8), 967–985. [https://doi.org/10.1130/0016-7606\(1983\)94<967:OOTTTA>2.0.CO;2](https://doi.org/10.1130/0016-7606(1983)94<967:OOTTTA>2.0.CO;2)